Buoyancy-Driven Circulation in an Ocean Basin with Isopycnals Intersecting the Sloping Boundary

ROBERT HALLBERG* AND PETER RHINES

School of Oceanography, University of Washington, Seattle, Washington

(Manuscript received 19 October 1994, in final form 11 October 1995)

ABSTRACT

The dynamics that govern the spreading of a convectively formed water mass in an ocean with sloping boundaries are examined using an isopycnal model that permits the interface between the layers to intersect the sloping boundaries. The simulations presented here use a two-layer configuration to demonstrate some of the pronounced differences in a baroclinically forced flow between the response in a basin with a flat bottom and vertical walls and a more realistic basin bounded by a sloping bottom. Each layer has a directly forced signal that propagates away from the forcing along the potential vorticity (PV) contours of that layer. Paired, opposed boundary currents are generated by refracted topographic Rossby waves, rather than Kelvin waves. It is impossible to decompose the flow into globally independent baroclinic and barotropic modes; topography causes the barotropic (i.e., depth averaged) response to buoyancy forcing to be just as strong as the baroclinic response. Because layer PV contours diverge, boundary currents are pulled apart at different depths even in weakly forced, essentially linear, cases. Such barotropic modes, often described as "caused by the JEBAR effect," are actually dominated by strong free flow along PV contours. With both planetary vorticity gradients and topography, the two layers are linearly coupled. This coupling is evident in upper-layer circulations that follow upper-layer PV contours but originate in unforced regions of strong lower-layer flow. The interior ocean response is confined primarily to PV contours that are either directly forced or strongly coupled at some point to directly forced PV contours of the other layer. Even when the forcing is strong enough to generate a rich eddy field in the upper layer, the topographic PV gradients in the lower layer stabilize that layer and inhibit exchange of fluid across PV contours. The dynamic processes explored in this study are pertinent to both nonlinear flows (strongly forced) and linear flows (weakly forced and forerunners of strongly forced). Both small (f plane) and large (full spherical variation of the Coriolis parameter) basins are included. Transequatorial basins, in which the geostrophic contours are blocked, are not described here.

1. Introduction

This study examines buoyancy-driven circulation in an ocean with sloping topography. Isopycnal surfaces intersect sloping topography at every ocean margin, but many of the prevalent ideas about the ocean circulation are based on models with vertical sidewalls. Boundary waves act as forerunners in setting up the boundary currents and in leveling, where possible, the density surfaces at the boundary (Wajsowicz and Gill 1986). The nature of these waves is strongly influenced by the continental rise, slope, and shelf, which produce a waveguide with much richer dynamics than exist with a vertical sidewall.

The classic approach to buoyancy-driven circulation (Stommel and Arons 1960) imagines the steady-state flow in a flat-bottomed basin that is driven by a localized mass source and a uniformly distributed mass sink. The interior flow is completely specified by continuity and a poleward flow to balance the potential vorticity (PV) forcing from the distributed upwelling. Viewed in the spherical domain, this poleward flow represents the preservation of the height of fluid columns measured parallel to the rotation axis (Rhines 1993). Western boundary currents provide the needed "plumbing" to close interior recirculations and feed the mass source into the interior at appropriate latitudes.

Kawase (1987) examines the development of linearized buoyancy-driven circulation in a flat-bottomed basin. He forces a $1\frac{1}{2}$-layer shallow water model with a localized mass source in the northwest corner of his basin and removes the mass with a Newtonian damping of the layer thickness anomaly; the vertical velocity at the layer top is greatest where the free-surface perturbations are largest. The mass source feeds a western boundary current, which follows a Kelvin wave down the western wall and across the basin at the equator,

* Current affiliation: Atmospheric and Oceanic Sciences Program, Princeton University, Princeton, New Jersey.

Corresponding author address: Dr. Robert Hallberg, Atmospheric and Oceanic Sciences Program, Princeton University, Sayre Hall, P.O. Box CN710, Princeton, NJ 08544-0710.

splits into northward and southward branches along the eastern boundary, and finally turns westward along the northern and southern walls. Along the eastern boundary, the poleward mass flux spreads into the interior following a long Rossby wave front. For sufficiently weak damping, his model develops into the circulation predicted by Stommel and Arons (1960), but for larger damping the circulation is arrested at an earlier state.

Rhines (1989), Straub and Rhines (1989), and Kawase and Straub (1991) extended these ideas to include isolated topography in $1\frac{1}{2}$-layer models of deep circulation. Although their topography is not large enough to penetrate the dynamically active layer, it is large enough to create closed PV contours. A broad pattern of upwelling induces a strong cyclonic circulation along closed PV contours over either a plateau or a depression. Steady flow along closed PV contours is a free mode; this mode has a resonant response to vortex stretching within the closed PV contours. Conversely, Rhines and MacCready (1989) and Rhines (1993) argue that a bowl-shaped basin driven by a heavy, sinking plume develops a large central region of anticyclonic circulation and vorticity in response to the horizontal divergence of fluid forced upward, displaced by the heavy plume. Cyclonic boundary currents are prominent at the rim of the bowl. There is some sign of large-scale anticyclonic circulation in the deep Pacific, both in observations (Johnson and Toole 1993) and in numerical simulations (Ishizaki 1994).

In other studies, Kawase (1993) finds that large circulations can develop along the closed PV contours of a bowl-shaped basin. The circulation is much weaker if the PV contours are blocked by the equator. Thompson (1995) examines the effect of topography on the quasigeostrophic flow that develops with eddies in a wind-driven basin. She finds that if the deepest layer includes closed PV contours, the circulation in that layer can remain quite robust in the final state, while in a basin without topography the analogous flow is essentially zero. These studies all indicate the profound influence that topographically induced closed PV contours can have on the ocean's circulation. Yet, the subtle interaction between baroclinity and bottom slope is not addressed by models with topography submerged in the lowest layer.

The large-scale response to buoyancy forcing has also been examined in three-dimensional models of the North Atlantic circulation. Gerdes and Köberle (1995) find a two stage response in the depth-averaged circulation to changes in the creation of deep water near Iceland in a primitive equation ocean general circulation model that is discretized into levels of fixed depth. The first stage is a change in the circulation along the western boundary, which is induced by coastal waves propagating away from the forcing region. The second stage is caused by an advective change in the properties of the deep water. Döscher et al. (1994) examine the response of the WOCE-CME model to changes in the forcing of deep-water production near the Nordic Seas. They also find a rapid deep response along the western boundary. The velocity perturbations of that response include the opposed pair of jets that are prominent in the present study. The boundary currents in these models tend to be characterized by a set of "double Kelvin waves" above the stair steps in the bottom. It is ironical that double Kelvin waves have vanishing group velocity and hence are very inefficient boundary propagators.

Isopycnal layer models may more accurately portray stratified flow near large amplitude topography. Several isopycnal layer models have recently been developed that allow layers to vanish or become arbitrarily thin (Hsu and Arakawa 1990; Bleck and Smith 1990; Oberhuber 1993). One of these models has been used to simulate flow past seamounts (Smith 1992). The present study uses an isopycnal model (described in the appendix) that permits isopycnals to intersect topography.

The numerical experiment presented here shows some aspects of the flow generated by buoyancy forcing in a basin with sloping sides that extend through the entire water column. The processes that are relevant in this system may also be important in the small basins where most of the deep water in the ocean is formed. The Labrador Sea is one such region that exhibits very strong boundary currents. In the Labrador Sea, there is a barotropic cyclonic flow that exhibits an annual maximum in strength in late spring, just after the period of deepest convection (Lazier and Wright 1993). This boundary current may be partially driven by conversion of convectively produced baroclinic flows into barotropic flow at the sloping western boundary, although it is certainly partially wind driven.

Localized buoyancy forcing drives the flow in this study. Buoyancy forcing is represented crudely by transferring fluid between layers, mimicking the adjustment of a convectively produced water mass. In a flat-bottomed basin, this forcing projects almost entirely onto the baroclinic modes. The classic barotropic (i.e., depth independent) and baroclinic modes over a level, flat bottom are no longer eigenmodes of the general sloping-bottom problem, which is in general nonseparable. The two vertical modes that do occur with uniform depth-gradient change in structure with the magnitude and direction of the thickness gradient. The result is, first, that buoyancy forcing no longer excites primarily classic baroclinic motions but also strongly drives depth-independent (classic barotropic) waves and flow, and second, that waves and flow can change in vertical structure as they propagate and advect around basins.

The local quasigeostrophic dispersion relation is used to trace the ray paths of the grave linear waves that spin up the flow. These ray tracing arguments provide an illustration of some of the same phenomenon observed in the isopycnal model simulations.

The first simulation, of buoyancy-driven flow in a basin with a flat bottom and vertical sidewalls, is included for comparison with the simulations of flow in a bowl-shaped basin. The vertical and horizontal structure of linear flow in such a basin are separable. Green's function for the quasigeostrophic flow on a β plane driven by a point source of PV is known for barotropic oscillatory forcing or steady forcing with a bottom friction (Rhines 1977; Rhines 1983) or steady, baroclinic diffusive flow (Gill and Smith 1970; Stommel 1982), and is called the beta plume.

The remaining simulations all depict flow in a bowl-shaped basin. The location of the buoyancy forcing is varied between the center of the basin and the northern edge of the basin, and this is found to have a significant impact on the flow that develops. Another simulation uses a constant Coriolis parameter and shows that the planetary vorticity gradient is vital for coupling the flow in the two layers. A final simulation, of the flow that develops with a greatly increased forcing, shows that topography acts as a strong barrier to the development of an eddy field and inhibits exchange of fluid across isobaths.

2. Ray tracing and the local dispersion relation

The simulations use the full primitive equations for two distinct layers. Still, most of the pertinent motions are well described by a quasigeostrophic balance, suggesting that a determination of the local dispersion relations for quasigeostrophic waves is useful. For infinitesimal perturbations to a two-layered resting fluid, these dispersion relations can easily be determined and used to trace the paths of the gravest rays, which spin up the flow.

The quasigeostrophic equations for two layers are

$$\frac{\partial}{\partial t}(\nabla^2\varphi_1 - \lambda_1^{-2}(\varphi_1 - \varphi_2)) + \boldsymbol{\beta}_1\cdot(\hat{\mathbf{z}}\times\nabla\varphi_1) = 0, \text{ and} \quad (1)$$

$$\frac{\partial}{\partial t}(\nabla^2\varphi_2 - \lambda_2^{-2}(\varphi_2 - \varphi_1)) + \boldsymbol{\beta}_2\cdot(\hat{\mathbf{z}}\times\nabla\varphi_2) = 0. \quad (2)$$

Equations (1) and (2) suppose that there are two layers with negligibly small horizontal velocities $\mathbf{u}_n = \hat{\mathbf{z}} \times \nabla\varphi_n$, thicknesses h_n and PVs $q_n \approx f/h_n$, separated by an interface with reduced gravity g', with a rigid-lid upper surface. Here $\lambda_n^2 = g'h_n/f^2$ is an internal deformation radius based on the thickness of layer n. The PV gradient times the thickness of each layer can be written as $\boldsymbol{\beta}_n = h_n\nabla q_n$. The PV gradients in the two layers differ because the lower-layer PV depends on the variable bottom topography. Several definitions make the final expression for the dispersion relation and vertical structure simpler. The total wavenumber is $K^2 = k^2 + l^2$. $\omega_n = [\hat{\mathbf{z}}\cdot(-\mathbf{k}\times\boldsymbol{\beta}_n)]/(K^2 + \lambda_n^{-2})$ is the frequency of Rossby waves based on the PV gradient and deformation radius of layer n. $R^2 = (K^2\lambda_1^2 + 1)^{-1} \times (K^2\lambda_2^2 + 1)^{-1}$, a measure of the wavelength compared with the layer deformation radii, goes from 0 (the short-wave limit) to 1 (the long-wave limit). Horizontal plane wave solutions to (1) and (2) with wavenumber $\mathbf{k} = k\hat{\mathbf{x}} + l\hat{\mathbf{y}}$ must satisfy

$$(\omega - \omega_1)(\omega - \omega_2) - (K^2\lambda_1^2 + 1)^{-1}(K^2\lambda_2^2 + 1)^{-1}\omega^2 = 0,$$

or

$$(1 - R^2)\omega^2 - (\omega_2 + \omega_1)\omega + \omega_1\omega_2 = 0. \quad (3)$$

The solutions to (3) give the dispersion relation for a horizontal plane wave

$$\omega = \frac{1}{2(1 - R^2)}[\omega_1 + \omega_2 \pm \sqrt{(\omega_1 + \omega_2)^2 - 4(1 - R^2)\omega_1\omega_2}]. \quad (4)$$

The two solutions described by (4) will be referred to as the positive and negative branch of the solution depending on the sign of the radicand. Equation (4) is only valid if the properties of the basin vary slowly on scales of the wavelength. Although this is not generally true in the simulations, the results of this analysis appear to make valid predictions for the full equations in a two-layer basin with large amplitude topography. The ratio of the velocities of the two layers for a solution of frequency ω is

$$\mathbf{u}_2 = (K^2\lambda_1^2 + 1)(1 - \omega_1/\omega)\mathbf{u}_1$$

or

$$\mathbf{u}_1 = (K^2\lambda_2^2 + 1)(1 - \omega_2/\omega)\mathbf{u}_2. \quad (5)$$

There is some redundancy in (4): the same solutions are described either by considering both branches of the dispersion relation only when they have positive frequency or by considering only one branch of the solution and retaining both positive and negative frequencies. Here both branches are considered, retaining only positive frequencies. The positive branch of (4) always has flow in the two layers in the same sense, while the negative branch has opposing flow in the two layers.

The dispersion relation, Eq. (4), gives the frequency of plane waves as a function of wavenumber at a given location. Figure 1 shows contours of four frequencies for a case where the lower-layer's PV gradient is five times as large as in the upper layer and rotated 45° from the direction of the upper-layer gradient. The topographic and planetary Rossby dispersion curves osculate at regions of common wavenumber and frequency, where a linear form of resonant interaction can occur between "modes" and the branch of the solution describing each mode switches. When the PV gradients of both layers are parallel, the positive and negative

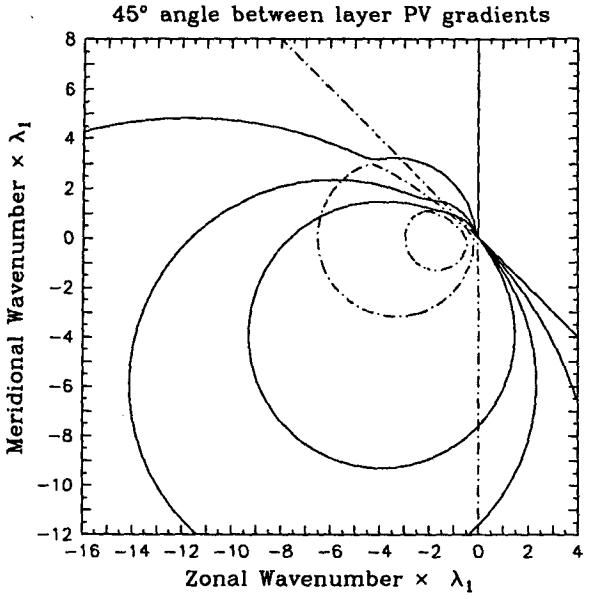

FIG. 1. Frequencies predicted by the dispersion relation, Eq. (4), for the lower-layer PV gradient five times as large as the upper-layer gradient and rotated by 45°. The negative branch of the dispersion relation is shown by dashed–dotted lines, while the positive branch is shown by solid lines. The lower layer is half as thick as the upper layer. The wavenumbers are scaled by the inverse of the upper-layer deformation radius λ_1. Four equally spaced frequencies (10^{-5}, 0.15, 0.3, and $0.45\beta_1\lambda_1$) are contoured for each branch of the solution, although the negative branch does not have frequencies as high as the largest contour value.

branches correspond to the barotropic and baroclinic modes. As the PV gradients are rotated with respect to each other, that simple description no longer holds. Both branches of the dispersion relation are needed to describe either layer's mode. When the layer PV gradients are rotated farther with respect to each other, more and more of the solution is described by just the positive branch of the dispersion relation, as seen in Fig. 2. Eventually, when the PV gradients are antiparallel, the entire solution is described by only the positive branch. As the negative branch solutions are pinched out by progressively larger angles between the PV gradients, the maximum frequency obtained by the negative branch decreases.

The dispersion relation (4) can be used for ray tracing in the two-layer basin. The ray is found by simultaneously solving the set of equations

$$\frac{Dx}{Dt} = \frac{\partial\omega}{\partial k}, \quad \frac{Dy}{Dt} = \frac{\partial\omega}{\partial l},$$

$$\frac{Dk}{Dt} = -\frac{\partial\omega}{\partial x}, \quad \text{and} \quad \frac{Dl}{Dt} = -\frac{\partial\omega}{\partial y}, \tag{6}$$

where the material derivative is defined as the derivative following the ray. These equations are integrated numerically. These equations exactly conserve frequency along a ray, and this property is used to validate the numerical integration.

For the bowl-shaped basin used in the simulations, ray paths are shown for a frequency of 5×10^{-8} s^{-1} (Fig. 3). These rays have a period of 1450 days, longer than the duration of the simulations, and are sufficiently grave to be representative of the waves that spin up the steady flow in the simulations. The rays in this figure initially have wavelength longer than 100 km, a quarter of the diameter of the forcing region in the simulations, and are uniformly distributed in wavenumber. This choice of the initial wavenumbers ensures that all of the rays will start with a westward or pseudowestward (for topographic waves) group velocity. The starting point for the upper panels are at the center of the forcing in the simulations. The lower panels' starting points were chosen to complement the upper panels.

The upper panels of Fig. 3 show the rays spreading in two distinct groups. One group, with its signal concentrated in the upper layer, radiates nearly westward from the forcing. The other group, with its signal concentrated in the lower layer, follows the topography around the basin. The rays in the center of each group propagate much more rapidly than those on the edges of the group, as seen by the density of the marks. The dashed line in Fig. 3 marks the edge of a "forbidden region" for the negative branch rays at this frequency. Outside this line, all of the negative branch solutions have lower frequency than the rays. In the south of the basin, the upper- and lower-layer PV gradients are in nearly opposite directions, and the negative branch attains only very low frequencies, as shown in Fig. 2. As the negative branch rays approach the forbidden region, they encounter a turning point. The rays stop and then propagate off to the west with most of their velocity transferred from the lower layer to the *upper* layer. The positive branch rays also reach turning points in the south and are transformed from lower-layer signals to upper-layer signals. The lower panels show ray paths starting to the east of the forbidden region. These ray paths also have two distinct groups. One group follows the topography around the basin, changing from being lower-layer intensified to being upper-layer intensified in the northern part of the basin. The rays in the other group propagate westward as upper-layer waves, reach turning points near the forbidden region, and then propagate eastward around the basin as lower-layer waves. The symmetry between the rays with turning points in the upper and lower panels is quite striking, suggesting that certain rays from the upper and lower panels may swap roles, and exchange energy, at their mutual turning points with negative branch solutions interacting strongly with positive branch solutions.

Rays with different frequencies behave similarly to those shown in Fig. 3. Higher frequency rays are less tightly confined to pseudowestward paths and have a larger forbidden region in the south. For frequencies low enough for planetary Rossby wave solutions to ex-

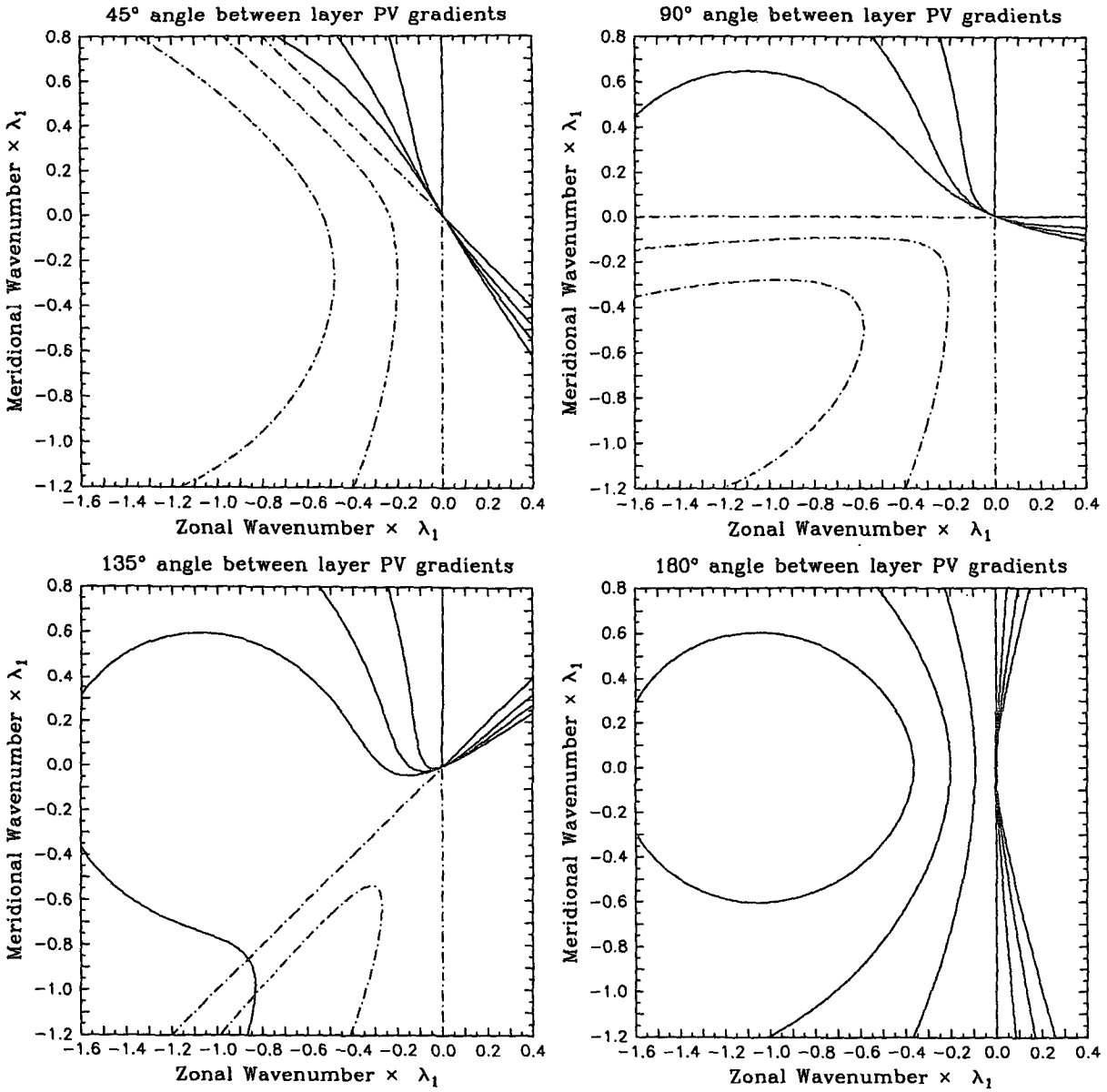

FIG. 2. As in Fig. 1 except that the region is limited to longer wavelengths and the angle between the two layer PV gradients is changed to 45°, 90°, 135°, and 180°. The same four frequencies are contoured in each panel. The positive branch of the dispersion relation is again contoured with solid lines, the negative branch with dashed–dotted lines.

ist, the rays will all have turning points at the edges of the forbidden region in the south.

The local modes in the two-layer case may not be typical in that their vertical structure is constrained by the layers. However, these layer solutions do illustrate the qualitative behavior of the continuously stratified case, which was described more fully by Rhines (1970) and Straub (1990) for special orientations between the bottom slope and the planetary vorticity gradient. In a continuously stratified rotating fluid, there is one mode that is bottom trapped and an infinite number of other modes in the vertical. These other modes are essentially baroclinic Rossby waves that have a horizontal-velocity node at the bottom, unless the flow is exactly aligned with isobaths. An important consequence of varying thickness is that the various (locally orthogonal) modes are not globally independent and they can exchange energy linearly, as described by Straub (1990).

3. The simulations

Five numerical experiments are described here. The parameters for these experiments are summarized in

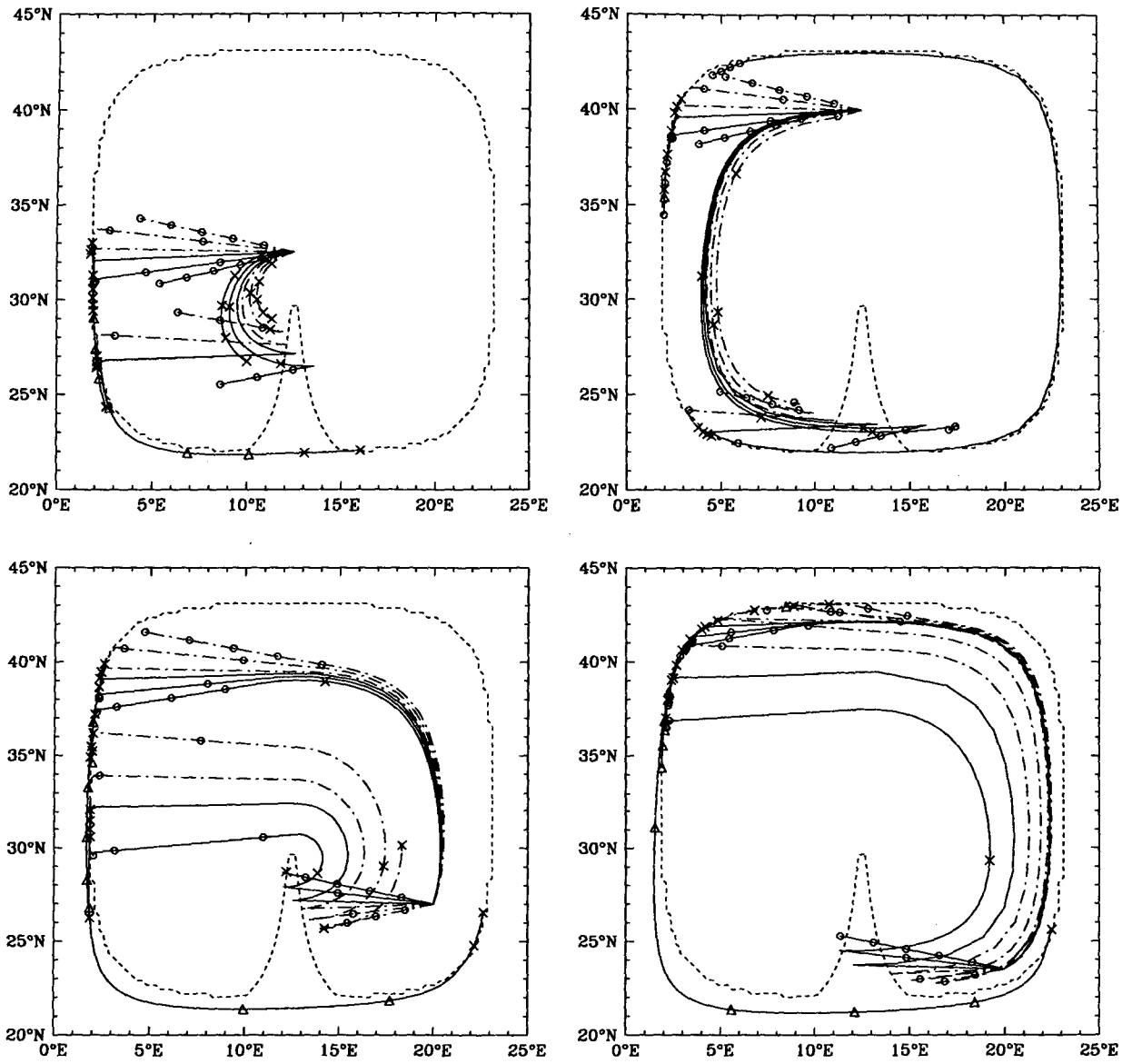

FIG. 3. Ray paths in the bowl-shaped basin for rays of frequency 5×10^{-8} s^{-1} for rays started at four locations: 32.5°N, 12.5°E; 40°N, 12.5°E; 27°N, 20°E; and 23.5°N, 20°E. The solid lines are rays from the positive branch of the dispersion relation, while the dashed–dotted lines are rays from the negative branch. The dashed line around the perimeter marks the region where the maximum frequency of the negative branch is less than the frequency of the rays. The negative branch rays cannot go outside this line. The rays go for 500 days, and the position every 100 days is marked. A circle is used as the mark if the upper-layer velocity is more than three times the lower-layer velocity. A cross is used if the lower-layer velocity is more than three times the upper-layer velocity. A triangle is used if the velocity in each layer is within a factor of three of the other.

Table 1. The numerical model solves the primitive equations in isopycnal coordinates and is described in the appendix. The basins are 25° wide, extending in latitude from 20° to 45°, with a grid resolution of 1/4°. In all cases, there are two layers with a maximum thickness of 750 m. Except in FLAT, the basin has sloping boundaries and a maximum depth of 1500 m. In FLAT, the basin has a uniform depth of 1500 m. The initial thicknesses for the simulations in bowl-shaped basins are shown in Fig. 4. The internal interface has a reduced gravity of 0.098 m s^{-2}, giving a baroclinic Rossby radius at the deepest point of 77 km, which is sufficiently resolved at about three grid points. The dominant eddy scales are several times the baroclinic Rossby radius. Discretized Rossby waves on a C grid (as in the present model) are a reasonable approximation to the continuous solution as long as there is at least one-half grid point per Rossby radius (Wajsowicz 1986). The small

TABLE 1. A summary of the simulations described in this study.

Section	Abbreviation	Basin shape	Forcing strength (Sv)	Forcing location	Coriolis parameter gradient at 30°N ($m^{-1}\ s^{-1}$)
4	FLAT	Flat bottom	0.0189	40°N, 12.25°E	1.98×10^{-11}
5	EDGE	Bowl shaped	0.0189	40°N, 12.25°E	1.98×10^{-11}
6	MID	Bowl shaped	0.0189	32.5°N, 12.25°E	1.98×10^{-11}
7	FPLANE	Bowl shaped	0.0189	40°N, 12.25°E	0
8	HIAMP	Bowl shaped	1.89	40°N, 12.25°E	1.98×10^{-11}

basin size and large internal Rossby radius were chosen so that all of the relevant scales would be well resolved in computationally tractable simulations. While this greatly reduces the timescales of the simulations, all of the processes described here are representative of the real ocean. Studies with higher horizontal and vertical resolution will eventually allow more complete representation of baroclinic modes.

Dissipation is included as an along-isopycnal biharmonic viscosity, with a coefficient of $10^{11}\ m^4\ s^{-1}$, and a vertical viscosity with a coefficient of $10^{-6}\ m^2\ s^{-1}$, approximately the molecular viscosity of water. The formulation for the viscosity is described in the appendix. The vertical viscosity is negligible for the timescales of the simulations unless a layer is thinner than about 100 m.

All simulations are forced with a circular cooling patch of uniform strength (parameterized as a volume transfer from the upper layer to the lower) and a radius of 200 km. The forcing is switched on at the beginning of the simulations and remains at the same intensity throughout. In MID the cooling patch is in the center of the basin. In the other four simulations, the cooling patch is near the northern slope but entirely contained in the region of finite lower-layer thickness. FPLANE differs from EDGE only in that the Coriolis parameter is held constant. HIAMP differs from EDGE only in that the forcing is 100 times larger. The flow that develops in HIAMP is strong enough to be nonlinear. Figure 4 shows initial contours of the upper- and lower-layer PVs for the three simulations in a bowl with varying Coriolis parameters (MID, EDGE, and HIAMP). In FPLANE, the resting PV contours are coincident with the thickness contours.

All of the simulations were run through the initial spinup, but the simulations do not reach final, statistically steady states. The cooled fluid is not returned to the upper layer via diapycnal mixing; these are spinup calculations, although many aspects achieve a quasi-steady state that should not change greatly when a diapycnal return flux is added. The kinetic energy plus available potential energy in FLAT stops increasing at about day 290, when dissipation in the western boundary becomes strong enough to balance the input of energy by the forcing and the upwelling is distributed throughout the basin. In the bowl-shaped basins, the thickness increase in the lower layer remains largely confined to the directly forced PV contours. The structure of the flow in the bowl-shaped basins attains a steady form but continues to intensify over time.

4. Flat bottom simulation (FLAT)

The spinup of the interior buoyancy-driven flow in a flat-bottomed basin is thoroughly understood from quasigeostrophic theory (Gill and Smith 1970; Rhines 1977). The boundary currents in a flat-bottom simulation are initiated by Kelvin waves, which have been extensively studied with $1\frac{1}{2}$-layer shallow-water models (Kawase 1987; Milliff and McWilliams 1994). This simulation is included primarily for comparison with the simulations in bowl-shaped basins.

The flow in FLAT is almost purely baroclinic. Figure 5 shows the transport streamfunction of the lower layer at days 100 and 1000; the upper-layer streamfunction is indistinguishable from the negative of the lower-layer streamfunction. The transport streamfunction ψ is found by solving the Poisson equation $\nabla^2\psi = \hat{\mathbf{z}}\cdot\nabla \times (h\mathbf{u})$, with $\psi = 0$ at the boundaries to satisfy the no normal flow boundary condition. Day 100 is in the middle of the spinup; by day 1000, the flow has attained its final form. The directly forced flow spreads west from the forcing as a beta plume following long baroclinic Rossby waves, reaching the western boundary at about day 150. At the western wall, a baroclinic Kelvin wave takes up the beta-plume mass flux. The beta plume is reflected as short Rossby waves at the western boundary, and the Kelvin wave radiates short Rossby waves as it propagates southward and spreads over progressively larger Rossby radii. The biharmonic friction dissipates these short Rossby waves, creating the biharmonic equivalent of a Munk boundary layer. When the Kelvin waves reach the eastern boundary, some of the mass flux is detrained into long baroclinic Rossby waves, which spread the mass source throughout the interior of the fluid. The development of the flow finishes after the eastern boundary current is strong enough to shed mass into the interior at the same rate as the forcing injects it. The combined kinetic and available potential energy stop increasing at this point, but the model never becomes steady because of the neglect of diapycnal mixing: the lower layer continues

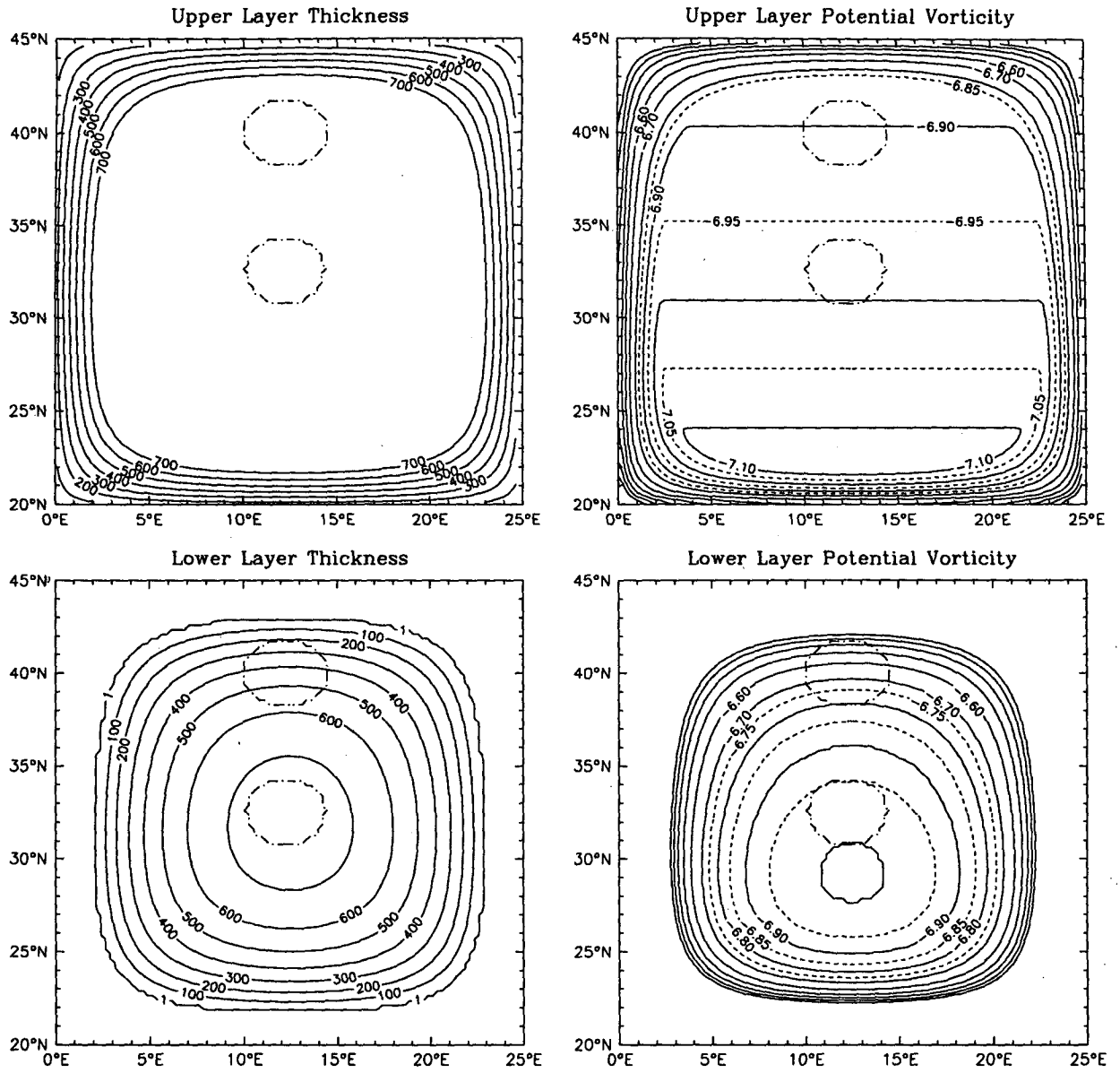

FIG. 4. Initial layer thicknesses (in m) (left) and $\log_{10}$ of initial layer PV (in $m^{-1} s^{-1}$) (right) for the two layers for the three simulations in a bowl-shaped basin with planetary vorticity gradients (MID, EDGE, and HIAMP). The simulations are forced in one of the two regions marked by dashed–dotted circles.

to increase in volume while the upper layer decreases. The Stommel–Arons (1960) steady interior circulation, which is driven by a uniform upwelling, is clearly seen in Fig. 6. This interior flow is vastly weaker than the directly forced beta plume.

The strength of the transport streamfunction can be predicted from an argument about the ratio of rotational to divergent transports. For divergent flow much weaker than rotational flow, a steady inviscid jet with velocity $\mathbf{u}$, width L, PV q, and a Bernoulli function difference ΔB across it, in a layer of thickness h, has a transport streamfunction difference of

$$\psi \approx -\mathbf{u}Lh = \Delta B/q. \tag{7}$$

Equation (7) is a generalized form of geostrophy and is an exact result of the steady, inviscid shallow-water equations for appropriate definitions of the PV and velocity of the jet. A localized mass source M can be carried away from the forcing by the difference in transport of a pair of opposed jets with the same Bernoulli function difference but different PVs, q_1 and q_2. An estimate for the difference in transport streamfunction across the source in the direction of long Rossby wave propagation results:

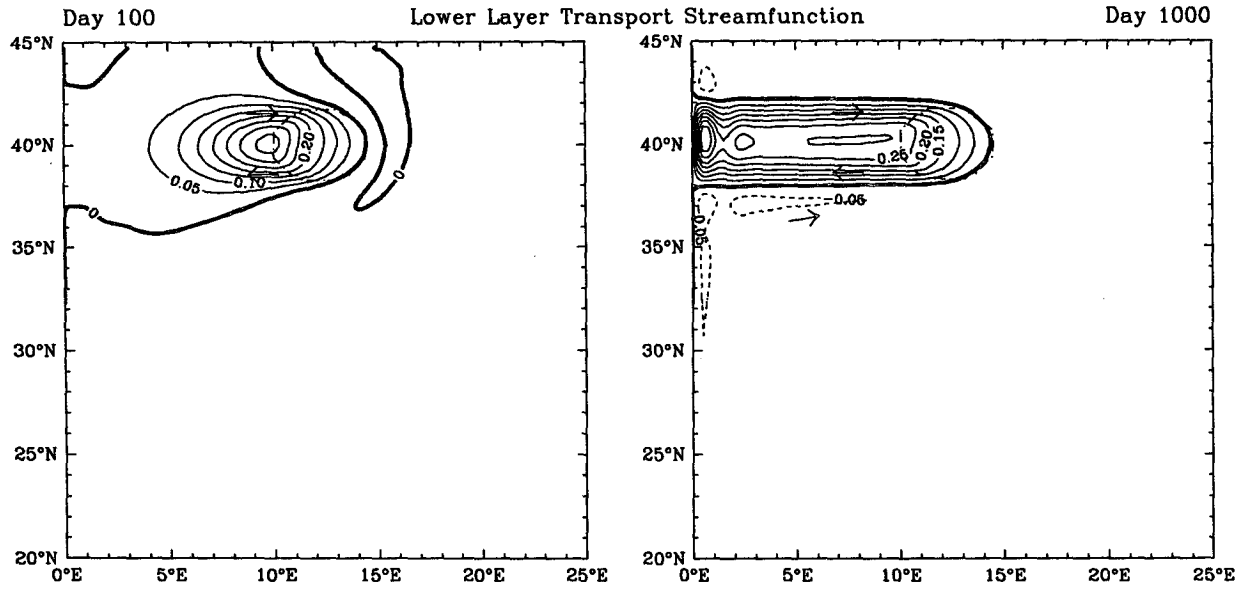

FIG. 5. Transport streamfunction of the lower layer (in Sv) at day 100 and 1000 of FLAT. The upper-layer flow is very nearly equal and opposite to the lower-layer flow. The dashed–dotted circles mark the forcing region. The arrows indicate the sense of the flow.

$$\Delta\psi/M \approx q/|q_1 - q_2|. \tag{8}$$

Equation (8) is a generalized version of the recirculation index of Rhines (1986); it arises from two distinct constraints on vertical velocity: one from the vorticity balance and the other from mass balance. For uniform layer thickness and linear flow, (8) becomes

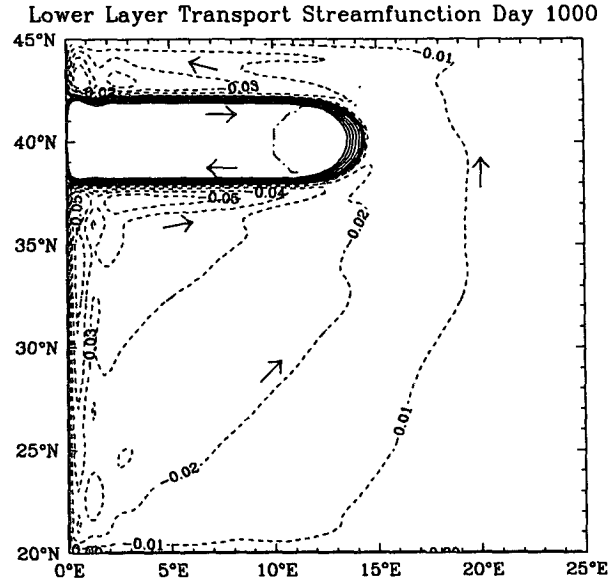

FIG. 6. Transport streamfunction of the lower layer (in Sv) at day 1000 of FLAT. This figure shows the same data as Fig. 5 but only includes contours from −0.05 to 0.05 Sv. The dashed–dotted circle marks the forcing region. The arrows indicate the sense of the flow.

$$\frac{\Delta\psi}{M} \approx \frac{f}{\beta L} = \frac{a}{L}\tan\theta, \tag{9}$$

where L is the meridional distance between the jets, a is the earth's radius, and θ is latitude. In the case of FLAT, (9) predicts a transport streamfunction that is amplified by a factor of 18 over the diapycnal transport forced by cooling (taking L to be 300 km). The result is a predicted transport streamfunction of the beta plume of 0.34 Sv (Sv $\equiv 10^6$ m^3 s^{-1}), in good agreement with the model transports in Fig. 5. Note that the streamfunction plots do not include the divergent part of the velocity field, which these arguments show to be small; the vector velocity plots represent the entire, divergent plus rotational, field.

The spinup can be examined dynamically by considering the layer-integrated PV balance:

$$\underbrace{\frac{\partial\zeta}{\partial t}}_{\substack{\text{Relative}\\ \text{vorticity}\\ \text{tendency}}} + \underbrace{-q\frac{\partial h}{\partial t}}_{\substack{\text{Eulerian}\\ \text{vortex}\\ \text{stretching}}} + \underbrace{h\mathbf{u}\cdot\nabla q}_{\text{PV advection}} = \underbrace{-qM - \nabla\times\left(\frac{A}{h}\{\nabla\cdot[h\nabla(\nabla^2\mathbf{u})]\}\right)}_{\text{forcing and dissipation}}. \tag{10}$$

Here ζ is relative vorticity, M is the diapycnal mass source for the layer (the forcing), and A is the biharmonic viscosity along isopycnals. The first term is the

tendency of relative vorticity. The second is the Eulerian portion of vortex stretching. The third is advection of PV, which comprises several terms

$$h\mathbf{u}\cdot\nabla q = \mathbf{u}\cdot\nabla f + \mathbf{u}\cdot\nabla\zeta - q\mathbf{u}\cdot\nabla h$$
$$\equiv \beta v + \mathbf{u}\cdot\nabla\zeta - q\mathbf{u}\cdot\nabla H - q\mathbf{u}\cdot\nabla h'. \quad (11)$$

The four terms on the right side of (11) are advection of planetary vorticity, advection of relative vorticity, topographically induced vortex stretching, and vortex stretching due to advection of dynamically induced layer thickness variations. For linear cases, advection of relative vorticity and advection of dynamic thickness variations are negligible. In FLAT, topographically induced vortex stretching is zero. [In bowl-shaped basins, planetary vorticity advection and topographically induced vortex stretching are of comparable magnitude and dominate the other terms in (10) if they are displayed separately.] The two terms on the right side of (10) are the forcing term and dissipation.

The balance of the terms dynamically differentiates several types of motion. Classic Rossby waves have relative vorticity tendency and Eulerian vortex stretching of the *same* sign, and both are balanced by PV advection. Conversely, for Kelvin waves relative vorticity tendency and Eulerian vortex stretching are of *opposite* sign and balance each other, with no signal in PV advection. For short Rossby waves, relative vorticity tendency is more important than vortex stretching, and vice versa for long Rossby waves. Relative vorticity tendency and vortex stretching are of comparable magnitude for Rossby waves with a wavelength of 2π times the Rossby radius. The Sverdrup balance has forcing balancing advection of planetary vorticity. The other balance found in these simulations is in the biharmonic Munk boundary layer, where dissipation balances PV advection. Topographic Rossby waves rely on vortex stretching due to upslope flow, but their relative vorticity tendency and Eulerian vortex stretching are in phase, like Rossby waves.

Figure 7 depicts the dynamical balances of the lower layer at day 200, during the spinup of the flat-bottom simulation, about 50 days after the beta plume reaches the western boundary. Note that the scale for Fig. 7 is roughly logarithmic but with positive and negative shades of corresponding magnitude. Forcing and dissipation are combined in Fig. 7d, but they can be separated easily, since the forcing pattern is a circular region of nearly uniform intensity and the biharmonic dissipation is only significant at small scales. The directly forced region shows that the Sverdrup relation holds, with PV advection (Fig. 7c) balancing forcing (Fig. 7d). Rossby waves are apparent near the forcing, with shorter waves spreading east and longer waves spreading west. Very short Rossby waves are dissipated around the forcing patch. Short Rossby waves predominate at the western boundary, completely masking the Kelvin wave signal. These short Rossby waves generate the Munk boundary layer as they are damped. Along the southern boundary and the eastern portion of the northern boundary, the Kelvin wave signal is clear, with Eulerian vortex stretching balancing relative vorticity tendency. Along the eastern boundary, long Rossby waves radiate into the interior. The long Rossby wave front extends farthest from the eastern boundary in the south, where the Rossby radius is largest and long Rossby waves propagate the fastest. The PV balance provides a thorough description of the spinup of the circulation in a flat-bottomed basin.

5. Flow in a bowl forced near the northern boundary (EDGE)

In this simulation the same forcing as in FLAT is applied to the bowl-shaped basin in Fig. 4. The beta plume is split into upper- and lower-layer plumes, each refracted to follow that layer's PV contours (Fig. 8). Paired, opposed boundary currents (Fig. 9) are initiated by bottom-trapped topographic Rossby waves. The upper- and lower-layer flows are linearly coupled but retain distinct identities.

The lower layer has a directly forced anticyclonic response that initially travels counterclockwise around the basin following a bottom-trapped Rossby wave along the lower-layer PV contours. This description is supported by comparing the apparent propagation speeds with the group velocity for bottom-trapped topographic Rossby waves. If the planetary PV gradient is negligible compared to the topographic PV gradient and the cross-slope wavenumber l is much larger than the alongslope wavenumber k, (4) becomes

$$\omega \approx -\frac{\beta_2\lambda_2^2 k(l^2\lambda_1^2 + 1)}{l^2(\lambda_1^2 + \lambda_2^2) + l^4\lambda_1^2\lambda_2^2}. \quad (12)$$

Using $\beta_2 = 3.8 \times 10^{-10}$ m^{-1} s^{-1}, upper- and lower-layer Rossby radii of 118 and 74 km, and a cross-slope wavenumber of 1.6×10^{-5} m^{-1}, (12) gives an alongslope group velocity of 0.95 m s^{-1}. (The baroclinic Kelvin wave speed is 4.6 m s^{-1}.) The bottom-trapped topographic Rossby waves considered here always propagate more slowly than baroclinic Kelvin waves. As pointed out by Rhines (1989), the group velocity of bottom-trapped topographic Rossby waves is ($N \sin\alpha/l$) in an f-plane ocean of constant stratification N, over a slope with angle α from the horizontal, with an across-slope wavenumber l that is much larger than the alongslope wavenumber. The group velocity of internal Kelvin waves is NH/π, where H is the depth of the fluid. The bottom-trapped topographic Rossby wave dispersion relation only holds if $\tan\alpha < f/N$ (for much steeper topography the Kelvin wave dispersion relation is recovered) and $NHl/f\pi \gg 1$. These two restrictions show that bottom-trapped topographic Rossby waves always propagate more slowly than internal Kelvin waves. With planetary vorticity gradients, the topographic waves are much more bottom intensified than on an f plane, and the bottom-trapped waves persist

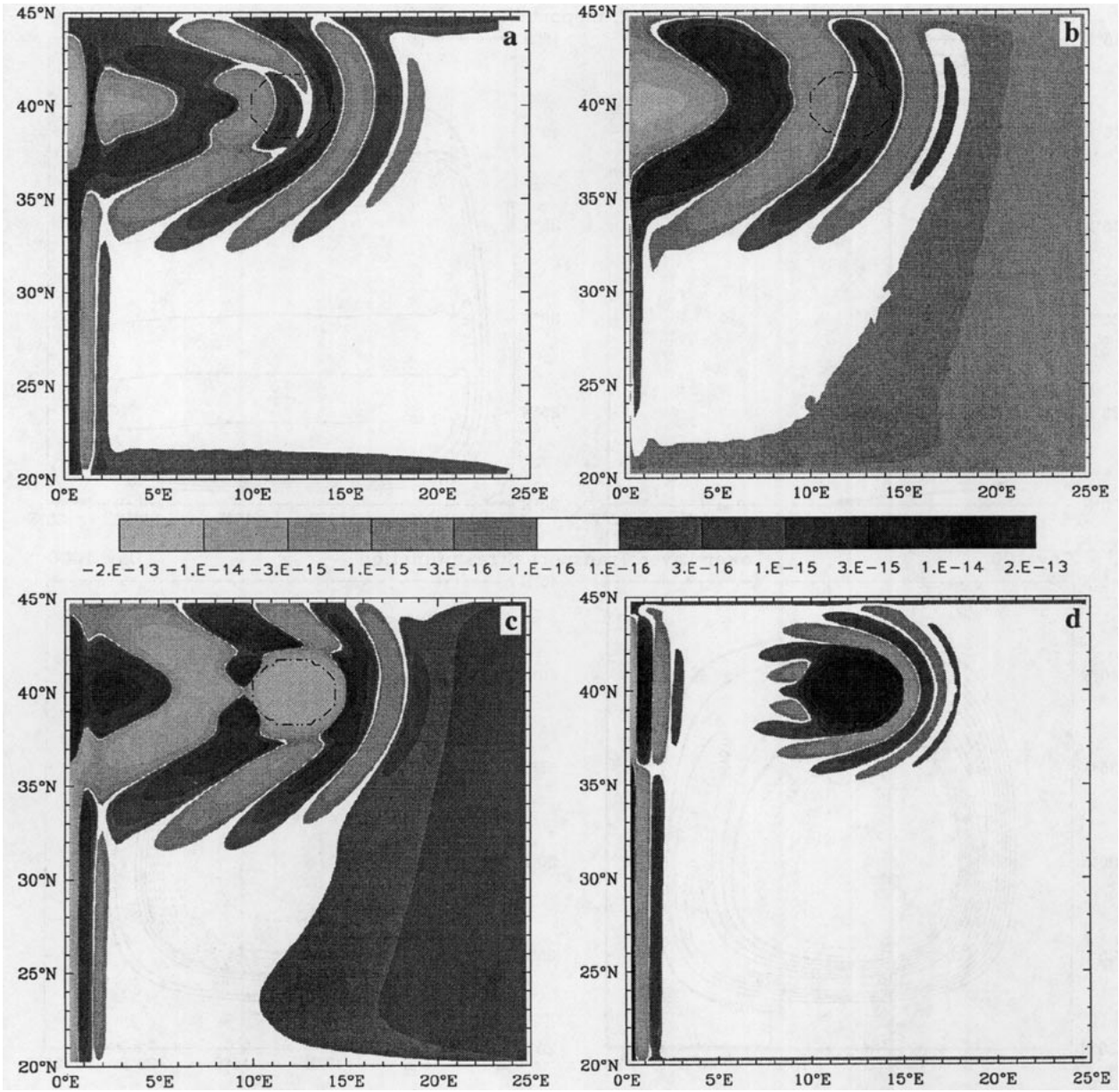

FIG. 7. Four terms in the PV balance of the lower layer at day 200 of FLAT. The terms are (a) relative vorticity tendency ($\partial\zeta/\partial t$), (b) Eulerian vortex stretching $[-q(\partial h/\partial t)]$, (c) PV advection ($h\mathbf{u}\cdot\nabla q$), and (d) combined forcing and dissipation. The dashed–dotted circles mark the forcing region.

even for much longer wavelengths than the internal deformation radius and still have slower group velocities than internal Kelvin waves.

Apparent group velocities for the lower layer can be obtained by examining plots of dynamically active fields as a function of time and pathlength along a lower-layer PV contour (Fig. 10). Pressure signals appear to propagate along the $10^{-6.6}$ m^{-1} s^{-1} PV contour with a group velocity of 1.2 m s^{-1}. By contrast, relative vorticity signals (which are more difficult to interpret because the intensity of relative vorticity changes along the path) seem to propagate along the same PV contour at about 0.5 m s^{-1}. Relative vorticity is more sensitive to smaller-scale motions than pressure is; relative vorticity is proportional to the horizontal Laplacian of pressure for geostrophically balanced flow. As shown by (12), propagation speeds increase with increasing cross-slope scales. Tangential velocities (velocities along the layer PV contours, which are close to along-slope velocities) indicate the across-slope structure of the spinup. The maximum tangential velocities are found along the $10^{-6.4}$ and $10^{-6.8}$ m^{-1} s^{-1} PV contours.

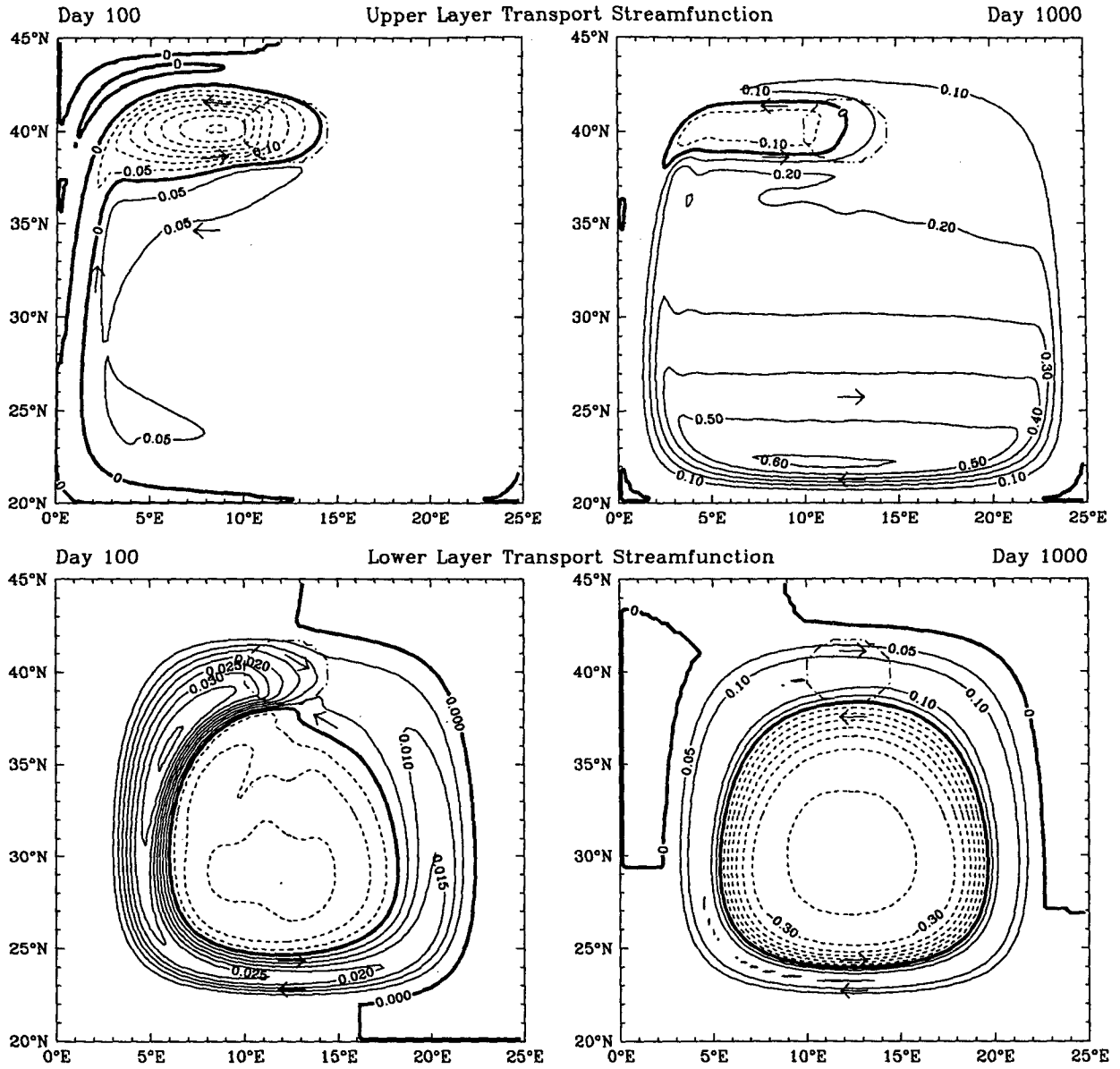

FIG. 8. Transport streamfunction of the two layers at days 100 and 1000 of EDGE (in Sv). The dashed–dotted circles mark the forcing region.

The apparent group velocity along the $10^{-6.8}$ m^{-1} s^{-1} PV contour is about 0.35 m s^{-1}, while along the $10^{-6.4}$ m^{-1} s^{-1} PV contour it is 0.9 m s^{-1}. The outer branch spins up more rapidly than the inner branch because it travels along a path of much greater slope.

The lower layer has a directly forced signal with an anticyclonic swirl that initially travels counterclockwise around the basin (Fig. 8). The response is along the same path taken by the rays in Fig. 3. The PV of the two directly forced jets lie along PV contours that differ in magnitude by a factor of about 2.5, so (8) predicts that the directly forced transport streamfunction should initially be only (at most) 1.7 times the strength of the volume input, or 0.033 Sv. This value is comparable with the model results and much weaker than in FLAT. The high pressure associated with the directly forced anticyclonic flow eventually forms a continuous band around the basin. The convergent flow that creates the high pressure is largely due to a weak outward velocity across the isobaths. The magnitude of the outward velocity is much less than the velocity along the isobaths. Inside and outside the central region of anticyclonic relative vorticity are bands of cyclonic relative vorticity (Fig. 11). This is precisely the relative

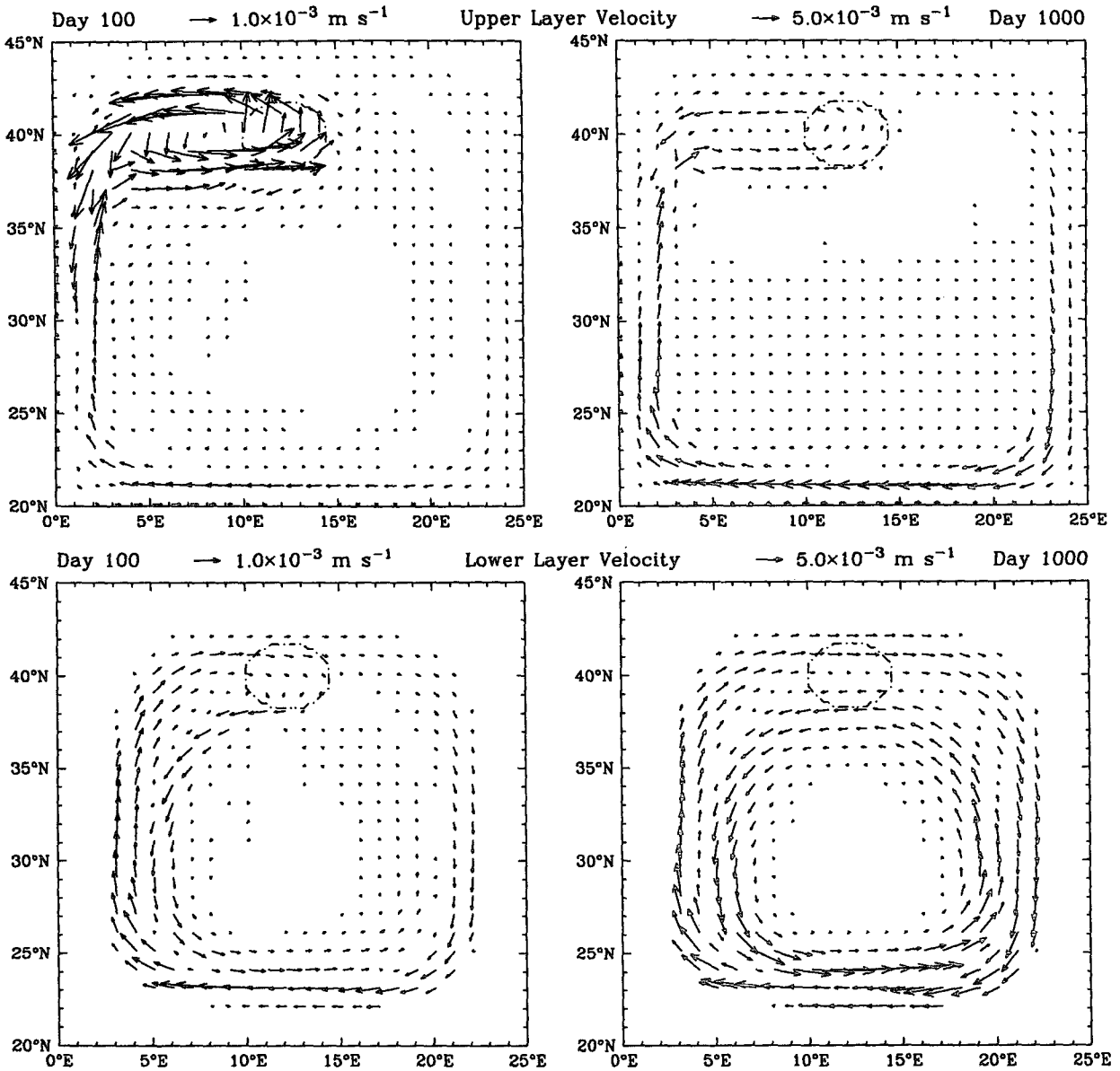

FIG. 9. Velocities of the two layers at days 100 and 1000 of EDGE. Every 16th point is plotted. Note that the velocity scale for day 1000 is much larger than for day 100. The dashed–dotted circles mark the forcing region.

vorticity structure of the beta plume but refracted to follow the lower-layer PV contours. In a flat-bottomed ocean the beta plume radiates westward from the forcing following grave planetary waves. As demonstrated by the ray tracing of section 2, the grave bottom-intensified waves in a bowl-shaped basin are refracted to follow the lower-layer PV contours. The flow in the lower layer is a thin ring of clockwise flow high on the slope around a thick region of counterclockwise flow of comparable magnitude lower on the slope. The transport streamfunction is initially predominantly anticyclonic because the outer jet develops more rapidly than the inner jet, but the final transport streamfunction is strongly cyclonic in the middle of the basin because the outer jet is in a much shallower region than the inner jet. The flow in the lower layer continues to increase linearly with time because the forcing imposes a pressure anomaly difference between the eastern and western sides of the forcing, and low-frequency bottom-trapped Rossby waves try to remove that pressure difference by carrying the pressure anomalies around the basin, approximately following lower-layer PV contours, from the west side of the forcing to the east side of the forcing. The rate of spinup is roughly $\partial\psi/\partial t$

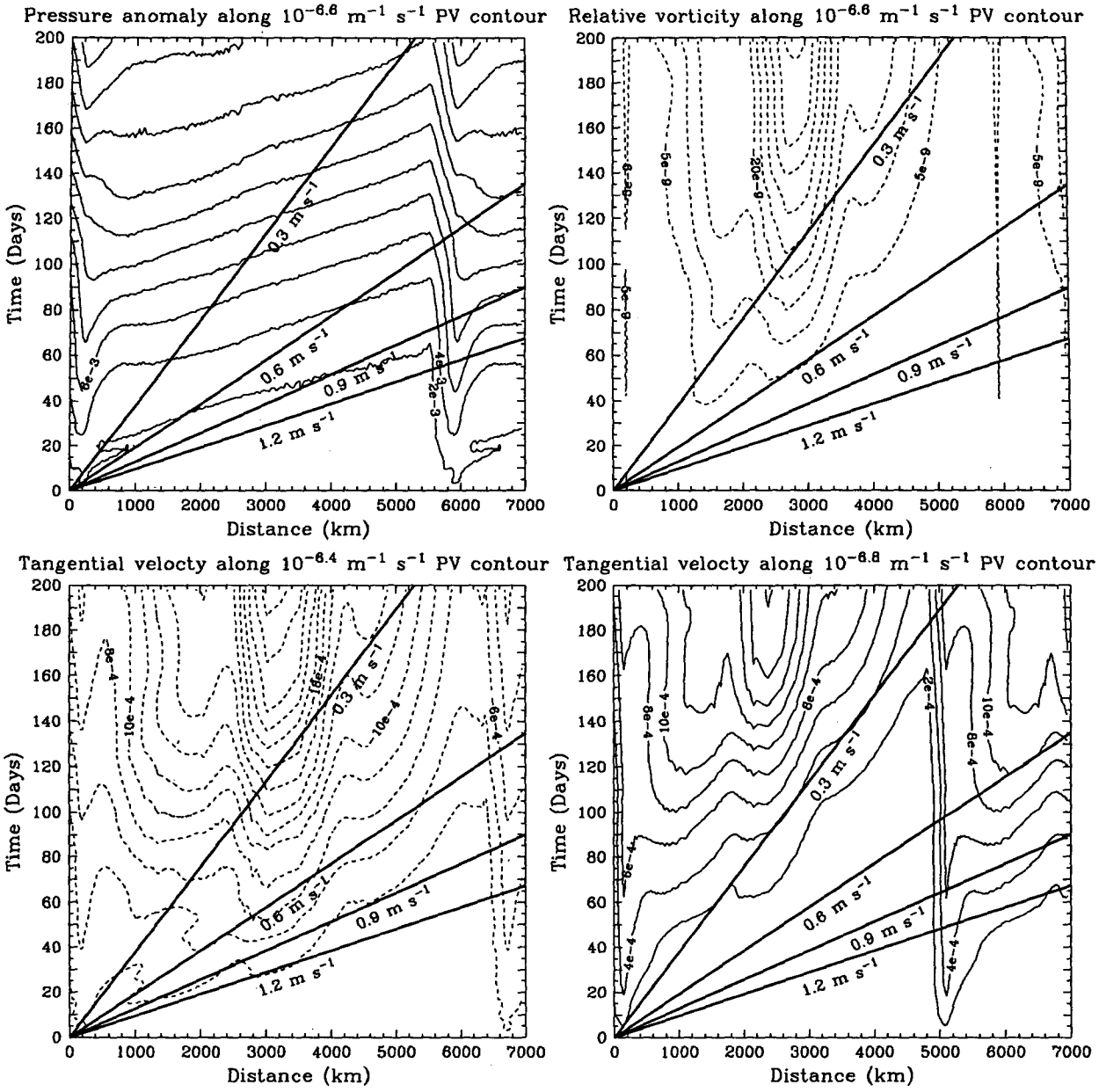

FIG. 10. Contours of several fields as a function of time and distance along a lower-layer PV contour (shown in Fig. 4). The lines give reference slopes. The paths in the upper plots repeat after 5700 km, and the lower left and right plots repeat after 6500 and 4900 km.

$\approx \Delta\psi/\tau$, where τ is the time required for bottom-trapped Rossby waves to propagate around the basin (50 to 100 days) and $\Delta\psi$ is the difference in streamfunction from the west side of the forcing to the east. (See, for example, the difference in streamfunction from 10° to 15°E along 39°N in the lower left panel of Fig. 8.) This argument neglects the possibility that coupling of the layers, described in section 2, retards the wave but gives a reasonable explanation of the actual lower-layer streamfunction at day 1000. The *pairs* of boundary currents that develop in this simulation are rather different in structure from the single edge intensified boundary current that occurs in FLAT.

The upper-layer response consists of a directly forced beta plume and a broad interior flow. The beta plume is of the same magnitude as in FLAT but turns equatorward near the western boundary rather than going straight into the wall. Within the ring of lower-layer thickening, the upper layer develops a strong anticyclonic circulation. This circulation results from vortex compression over the thickening portions of the lower layer. This initial response to thickening can be seen,

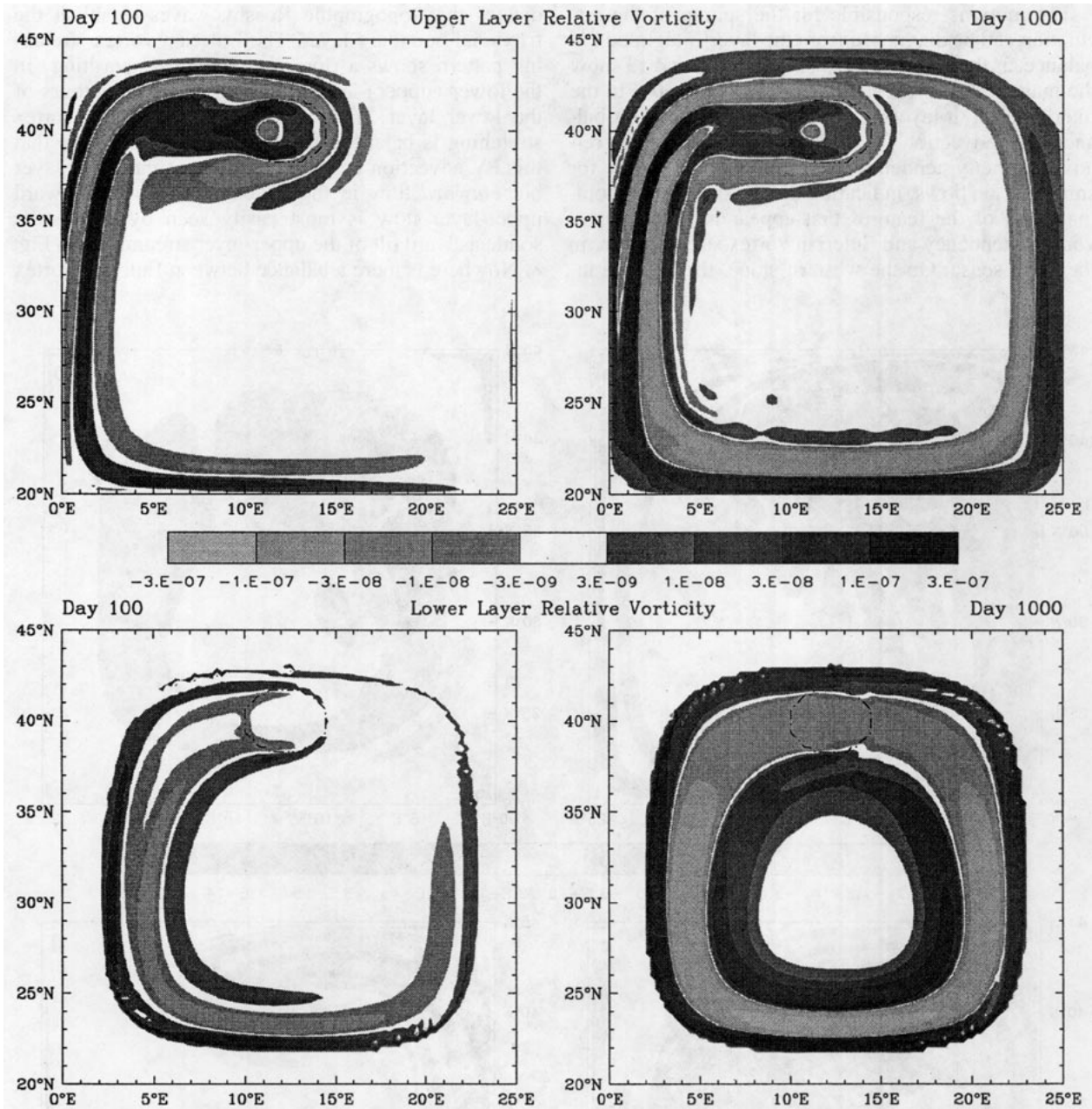

FIG. 11. Relative vorticities (in s^{-1}) of the two layers at days 100 and 1000 of EDGE. Note that the scale is roughly logarithmic. The dashed–dotted circles mark the forcing region.

for example, in the band of southward flow at 20°E at day 100 in Fig. 9. The anticyclonic response in the upper layer to thickening in the lower layer propagates westward in the interior, then southward and eastward along the slope following the upper-layer PV contours shown in Fig. 4. By the end of the simulation there is a broad anticyclonic circulation throughout all of the upper layer except for the directly forced beta plume. The velocities are the largest along the southern slope, where the PV contours are constricted. Another simulation (not included here) was done with only the upper layer, and it was found that the anticyclonic interior flow is about twice as strong when the lower layer is included, indicating a strong hypsometric contribution. The interior circulation eventually feeds mass to the sink in the north through a broad *eastward* flow in the interior, which feeds a strong *eastern* boundary current. The eastern boundary current flows southward to become a southern, and eventually western, boundary current.

The motions responsible for the spinup of the circulation can be diagnosed from the layer-integrated PV balance, as they were in FLAT. Figures 12 and 13 show the magnitudes of the various terms from (10). In the interior of both layers, Eulerian vortex stretching balances PV advection for the broadest flows, while relative vorticity tendency balances PV advection for smaller scale flows, indicating that Rossby waves dominate. All of the features that appear in both relative vorticity tendency and Eulerian vortex stretching are in the same sense. On the western slope, the balance indicates that topographic Rossby waves establish the frictional boundary layer. The Eulerian vortex stretching pattern shows a ring of stretching (squashing) in the lower (upper) layer following the PV contours of the lower layer. In both layers this Eulerian vortex stretching is balanced by PV advection, but note that this PV advection is southward flow in the upper layer but *outward* flow in the lower layer. The southward upper-layer flow is most easily seen by noting the southeastward tilt of the upper-layer streamlines in Fig. 8. Nowhere is there a balance between Eulerian vortex

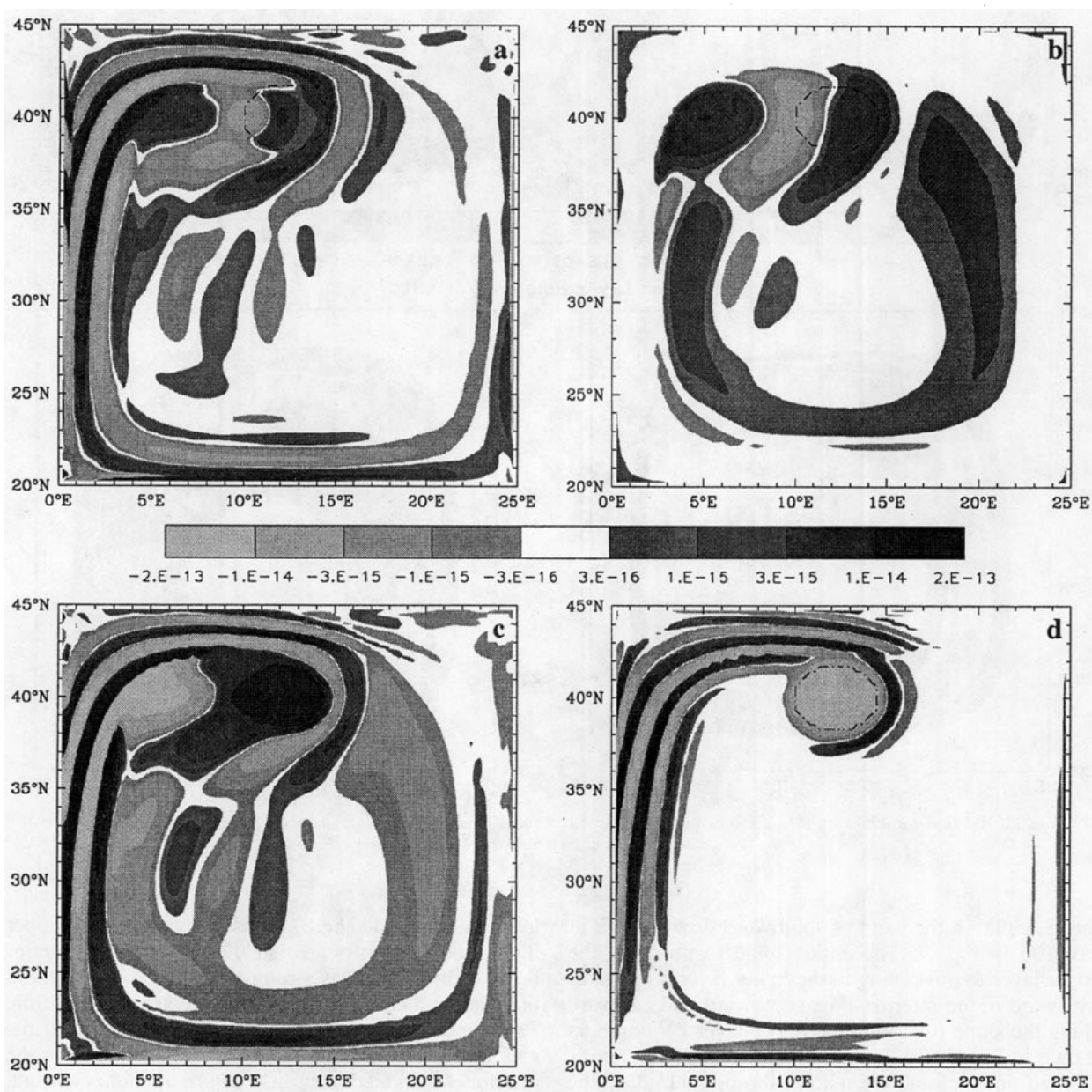

FIG. 12. Four terms in the PV balance of the upper layer at day 100 of EDGE. The terms are (a) relative vorticity tendency ($\partial\zeta/\partial t$), (b) Eulerian vortex stretching $[-q(\partial h/\partial t)]$, (c) PV advection ($h\mathbf{u}\cdot\nabla q$), and (d) combined forcing and dissipation. The dashed–dotted circles mark the forcing region.

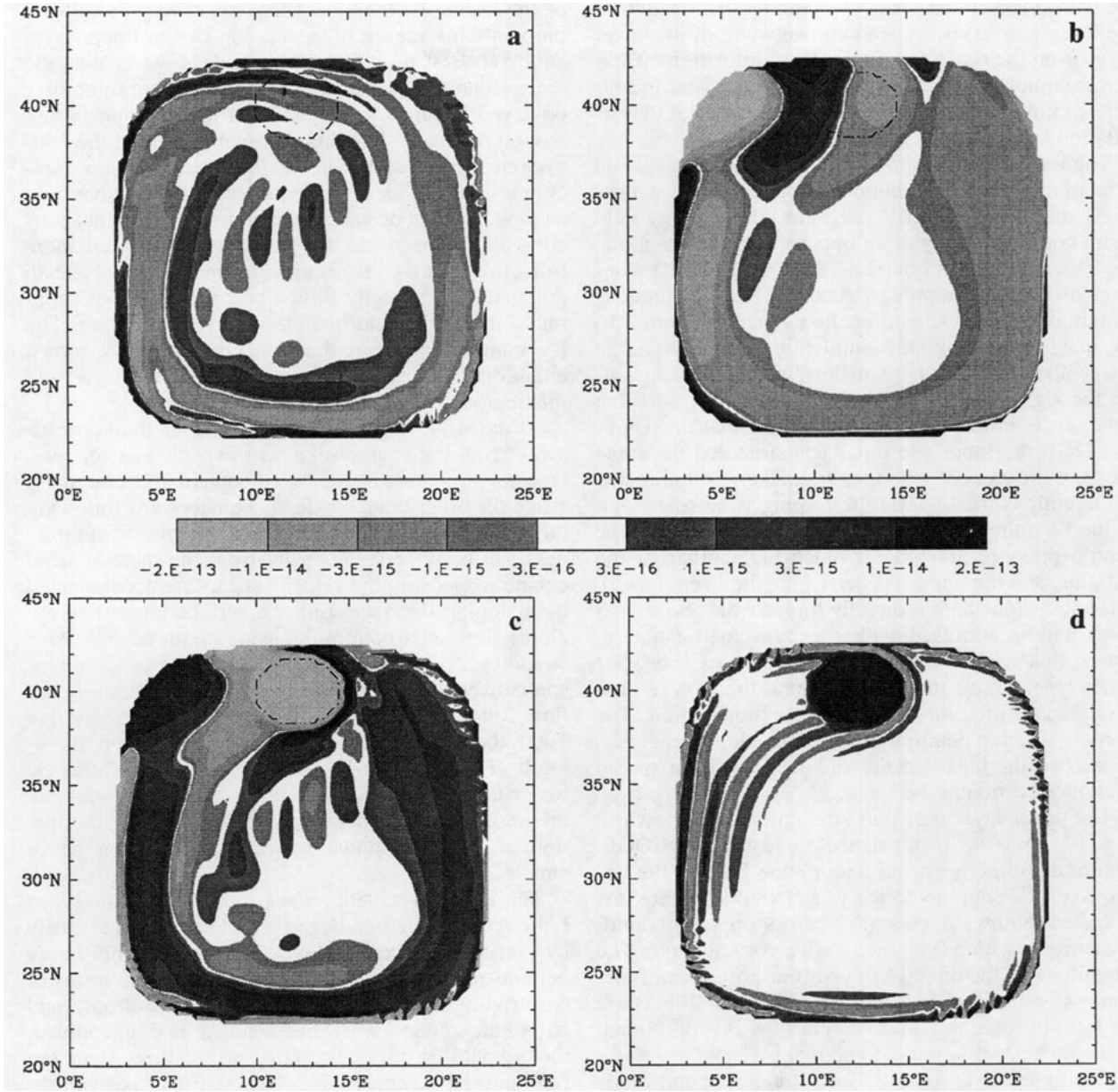

FIG. 13. Four terms in the PV balance of the lower layer at day 100 of EDGE. The terms are (a) relative vorticity tendency ($\partial\zeta/\partial t$), (b) Eulerian vortex stretching [$-q(\partial h/\partial t)$], (c) PV advection, and (d) combined forcing and dissipation. The dashed–dotted circles mark the forcing region.

stretching and relative vorticity tendency that would indicate the presence of Kelvin waves. The role of the Kelvin waves in FLAT is assumed by bottom-trapped and topographic Rossby waves (Rhines 1970).

This simulation demonstrates the profound differences that the large amplitude topography causes on the flow that develops as a result of buoyancy forcing. The role that baroclinic Kelvin waves played in FLAT is taken up by bottom-trapped Rossby waves. The two layers spin up following separate signals, with only a weak expression of the flow in the opposite layer, since the cross-jet scales are comparable to the internal Rossby radius. The upper- and lower-layer flows interact, even in the linear wave limit but retain their distinct character in most of the basin.

6. Basin center forcing in a bowl-shaped basin (MID)

This simulation differs from EDGE only in the location of the forcing; it is at the center of the basin rather than the edge. Many of the dynamic processes

are the same as in EDGE, but changing the location of the forcing reverses the predominant swirl of the lower layer from the sense in EDGE. This simulation clearly demonstrates the coupling between layers and the inapplicability of a barotropic–baroclinic view of the circulation.

The lower layer again spins up with an anticyclonic beta plume following bottom-trapped Rossby waves along the lower-layer PV contours. The velocity field again consists largely of an opposed pair of jets along the PV contours that bound the forcing. These PV contours differ in magnitude by about 12%, so (8) predicts an initial transport streamfunction signal of about 0.16 Sv, in agreement with the simulation. As in EDGE, the lower-layer circulation intensifies linearly with time after the signal circles the basin, but the net swirl that develops is in the opposite sense from that in EDGE. In EDGE the inner and outer jets straddled the same pressure difference, so the inner, thicker jet dominated the overall swirl. In MID the forcing is close enough to the PV minimum in the center of the basin that the central pressure anomaly is much higher than at the margins, and the outer jets determine the overall swirl. The anticyclone here is directly forced from above, and must not be confused with the hypsometric anticyclones that can be forced by underflow of a heavier water type. Notice that the dominant direction of flow is opposite to the direction of wave propagation. The vorticity forcing determines the anticyclonic tendency, counter to the idea that the sinking fluid must spread cyclonically around the basin.

The upper-layer transport streamfunction, shown in Fig. 14, spins up in much the same way as EDGE. Again, the directly forced beta plume follows the upper-layer PV contours to the western slope, where it is refracted southward, creating a pair of opposed boundary currents with a cyclonic relative vorticity core. The magnitude of the directly forced transport streamfunction is slightly smaller than in FLAT or EDGE because the ratio of rotational to divergent flow is proportional to the tangent of latitude, as shown by (9).

The upper-layer velocity and streamfunction fields (Fig. 14 and Fig. 15) also show a broad anticyclonic circulation that fills the basin to the south of the main cyclonic beta plume. This anticyclone is a basinwide response to the geographically small region of forcing. It is much stronger in transport and velocity (particularly at the rim) than is the Stommel–Arons flow in FLAT. The anticyclone is due to the hypsometric effect of Rhines and MacCready (1989), in which bowl topography causes upward flow to develop horizontal divergence and, hence, anticyclonic Kelvin circulation. In the presence of closed PV contours, this response is particularly strong.

Ray tracing provides a complementary explanation of the spinup of the upper-level circulation. The rays depicted in Fig. 3 convert from lower-layer modes to upper-layer modes in the equatorward-central quadrant of the basin. To the extent that ray theory is valid, it pinpoints the region of generation of the upper-layer anticyclone. It must be emphasized, however, that the scale separation required by the theory is not rigorously observed. Boundary jets are seen to penetrate farther around the basin than this theory allows, and the anticyclone fills out all the way to the eastern margin. Nevertheless, these ideas begin to make the elusive connection between deep boundary currents and global circulation response. As the simulation spins up more fully, this upper-layer response to forcing from beneath dominates the directly forced beta plume in determining both interior and boundary current structure. The PV contours north of the beta plume are not forced either directly or by coupling with the lower layer, and this region remains largely at rest.

At day 100, the excess of lower-layer fluid spreads away from the source region in two distinct tongues. One tongue extends westward toward the boundary, while the other branch extends equatorward following the lower-layer PV contours. This distribution of thickness can be understood easily from the thermal wind equation. Geostrophic velocity shears are accompanied by a sloping interface. Either a surface-intensified cyclonic flow or a bottom-intensified anticyclonic swirl straddles a region of thickened lower layer. Comparison between Fig. 16 and Fig. 4 shows how closely the flow follows one of the layer's PV contours. By day 1000, the thickness anomaly is concentrated on the directly forced lower-layer PV contours. While the lower-layer circulation increases steadily in strength, the upper-layer signal's strength is limited by dissipation along the boundaries where the motion has a smaller scale.

The depth-averaged velocity, shown in Fig. 17, is rather complicated and can be understood most easily by considering the two layers separately. This figure demonstrates the limited value of thinking in terms of barotropic and baroclinic flow. If the barotropic and baroclinic modes were independent and uncoupled, there would be only a weak barotropic flow, since the forcing is largely baroclinic. Indeed, FLAT has vanishingly weak barotropic circulation. In the simulations with topography, the barotropic flow is of the same magnitude as the baroclinic flow. This physical system is not separable into two globally discrete modes, and it is not particularly meaningful to speak in terms of a barotropic and baroclinic flow.

This simulation concurs in many ways with EDGE. Paired boundary currents are again initiated by Rossby waves, but the sense of the net lower-layer swirl is reversed by the changed forcing location. The upper layer demonstrates the linear coupling between the layers in the region of antiparallel topographic and planetary vorticity gradients, as indicated by the ray tracing in Fig. 3. The depth-averaged flow is large and has a complicated spatial structure, despite a simple baroclinic forcing, indicating the inadequacy of barotropic and

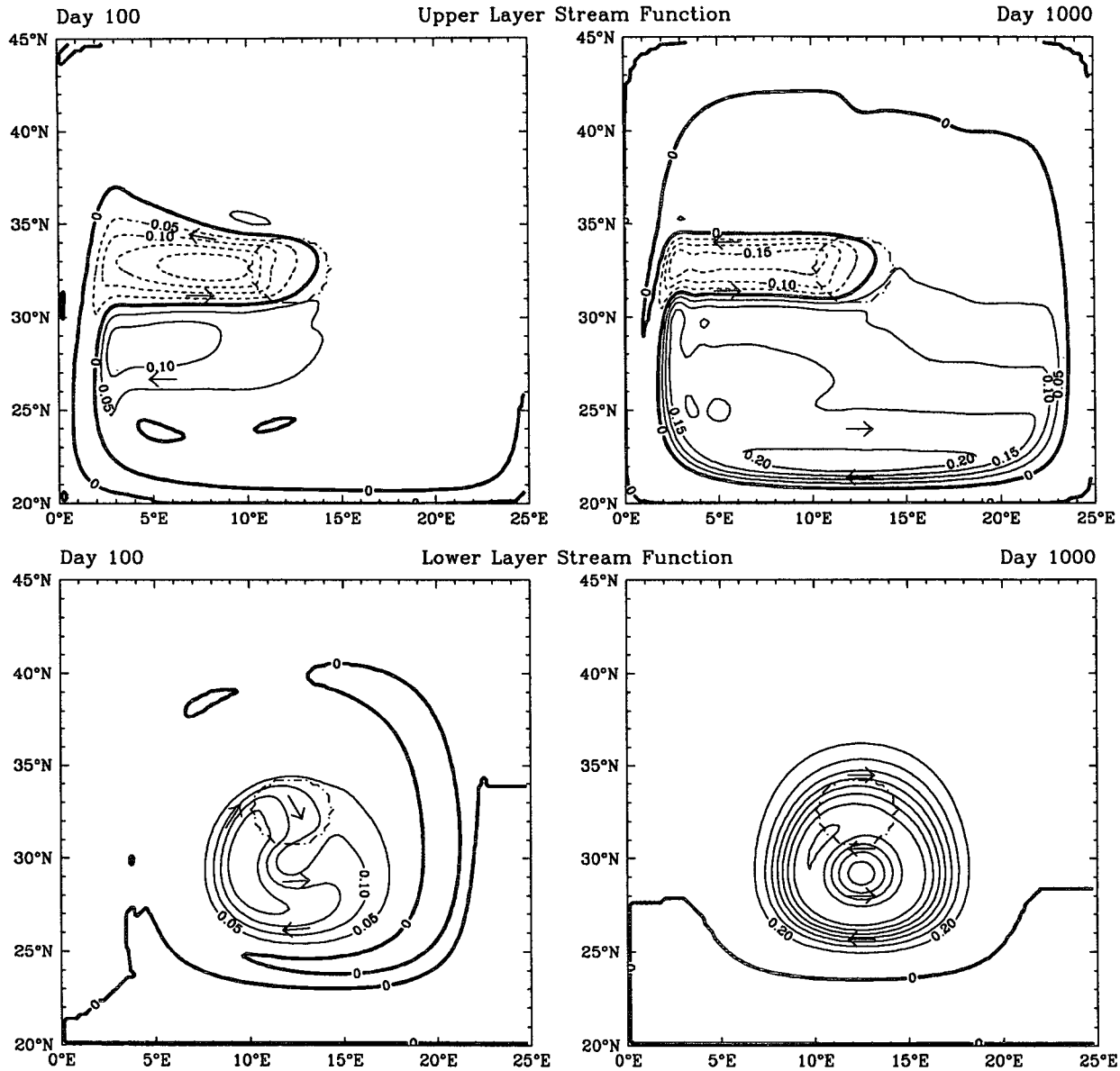

FIG. 14. Transport streamfunction of the two layers at days 100 and 1000 of MID (in Sv). The dashed–dotted circles mark the forcing region. The arrows show the sense of the flow.

baroclinic descriptions of this simulation. The spinup and structure of the circulation are much more easily described in terms of the flow in each layer.

7. Flow in a bowl without planetary vorticity gradients (FPLANE)

This simulation illustrates the importance of planetary vorticity gradients in determining the nature of the flow. This simulation is identical to EDGE except that the Coriolis parameter is held constant. This one change drastically alters the development of the flow and eliminates the coupling between upper- and lower-layer intensified flow.

The lower-layer transport streamfunction for this simulation (Fig. 18) has only minor differences from EDGE. Extremely large differences between the two simulations appear in the upper-layer flow. The upper-layer streamfunction is largely expressed in a directly forced geostrophically adjusted cyclone. The anticyclonic streamfunction in the upper layer is the projection of a bottom-trapped mode onto the upper layer and does not indicate that coupling between modes has occurred. (The transport streamfunction is larger in the

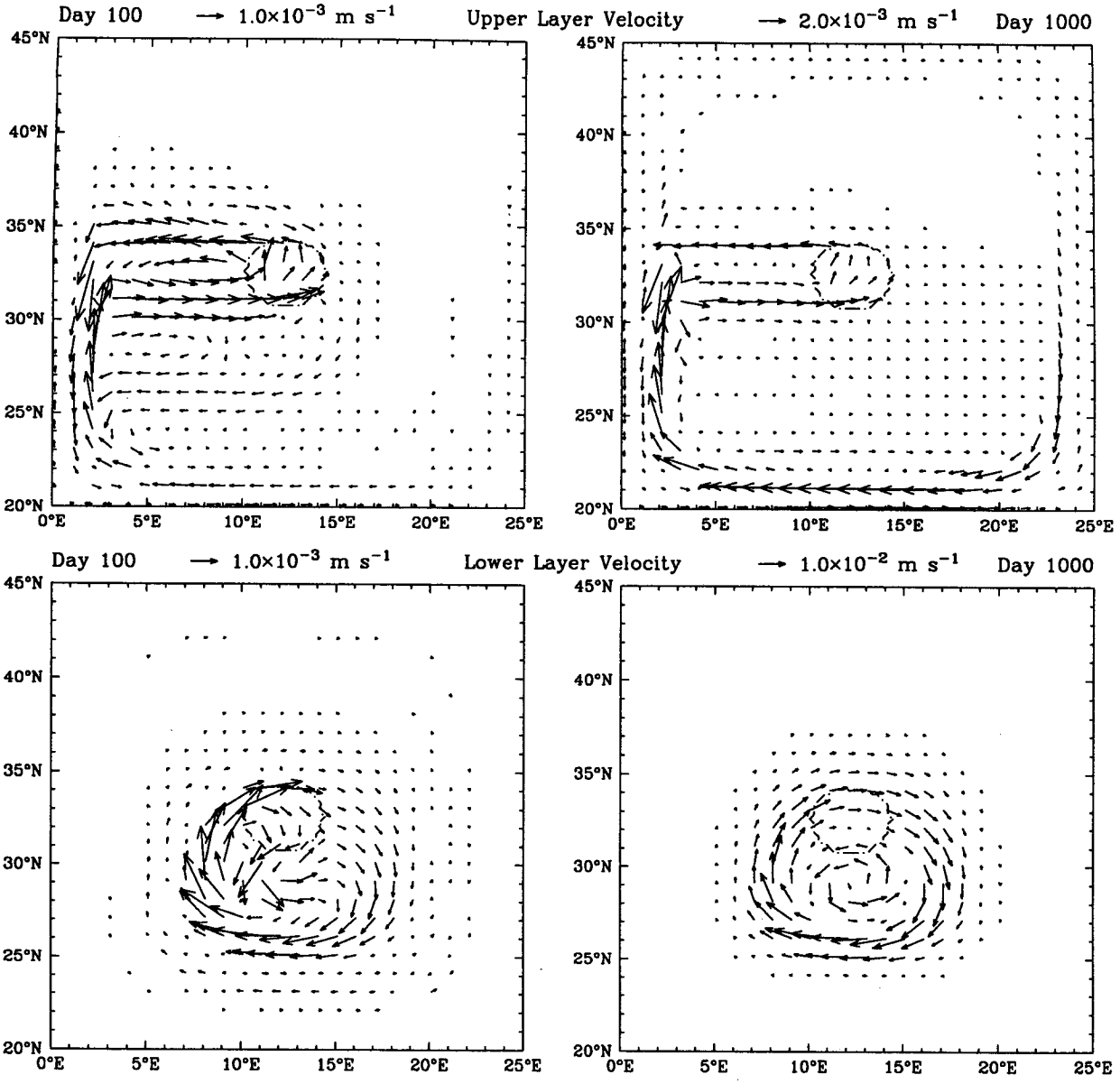

FIG. 15. Velocities of the two layers at days 100 and 1000 of MID. Every 16th point is plotted. Note that the scale is different for each plot. The dashed–dotted circles mark the forcing region.

upper layer, but the velocities are larger in the lower layer.) Without planetary vorticity gradients the circulation can be decomposed into two globally independent vertical modes. One of the modes consists of steady geostrophically balanced upper-layer flow and does not propagate. (On an f plane, any steady geostrophically balanced upper-layer flow is an exact solution of the linear inviscid equations of motion.) In the dispersion relation derived in section 2, one of the solutions has identically vanishing frequency and no flow in the lower layer. The other solution's motions are expressed more strongly in the lower layer and spinup following bottom-trapped Rossby waves or topographic Rossby waves along isobaths. The steady geostrophically balanced mode is forced about twice as strongly as the propagating mode. Even though the flow in this simulation is separable into independent modes, the depth-averaged velocity is still quite large, indicating that topography alone, without planetary vorticity gradients, is able to disturb a barotropic–baroclinic description of the circulation.

This simulation without planetary vorticity gradients shows that even though the topographic gradients of PV are much stronger than gradients of planetary vor-

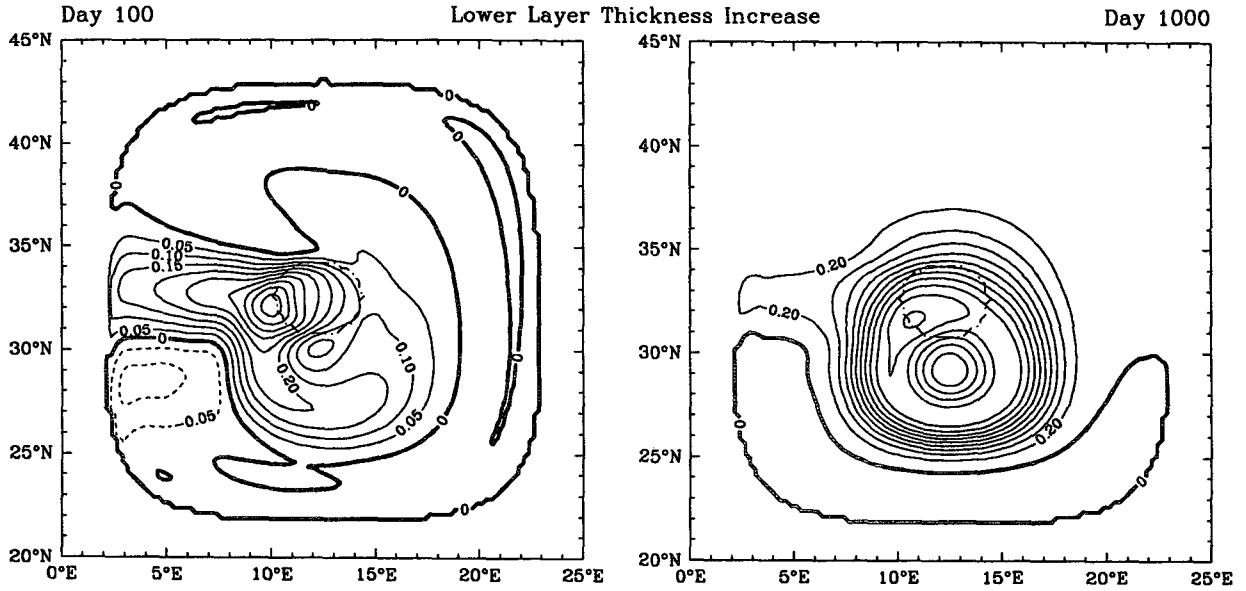

FIG. 16. Lower-layer thickness increase (in m) by days (a) 100 and (b) 1000 of MID.

ticity, a nonconstant Coriolis parameter is still important in determining the character of the flow (compare Fig. 18 with Fig. 8). This result has direct bearing on the possibility of simulating intermediate water circulation in the laboratory. In the laboratory the only PV gradients that can be generated are due to topography, and it may be difficult to attain pertinent results for the problem of the large-scale intermediate water circulation. Of course, at higher amplitude the f-plane response is more elaborate, involving mesoscale eddies and baroclinic instability. The effect of a strong mesoscale on the launching of boundary currents is of great interest. We have conducted similar experiments in the laboratory, and these experiments seem to verify the general features of this simulation.

8. Large amplitude flow in a bowl forced near the northern boundary

In all of the preceding simulations, the model was forced very weakly. Reversing the sign of the forcing,

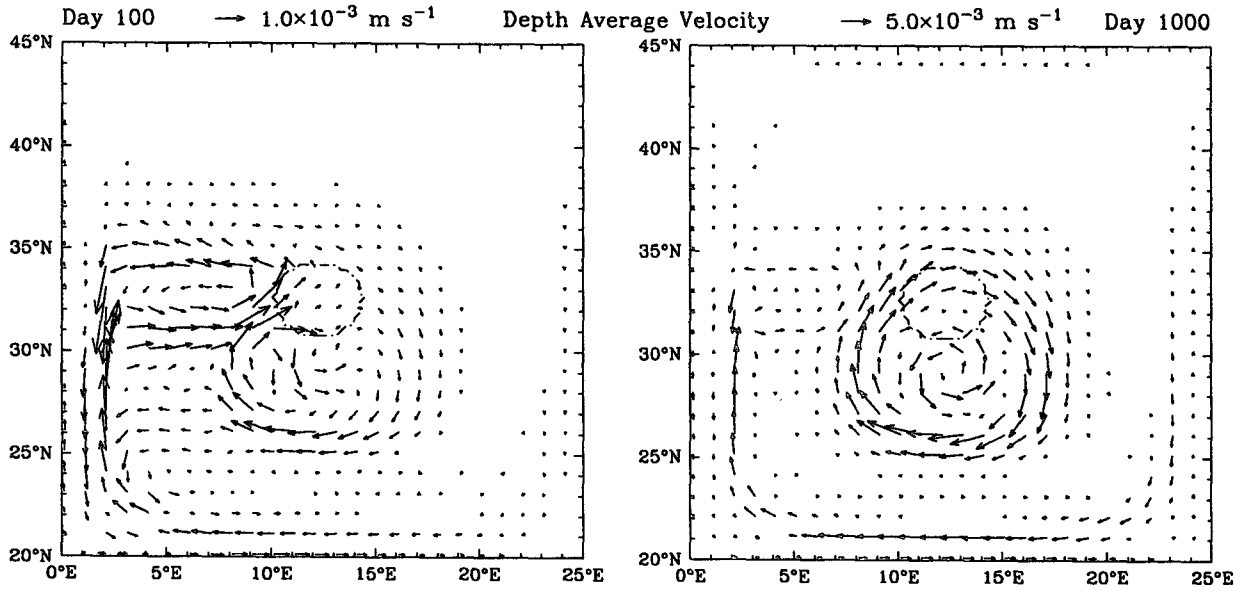

FIG. 17. Depth-average velocities at days (a) 100 and (b) 1000 of MID. Every 16th point is plotted.

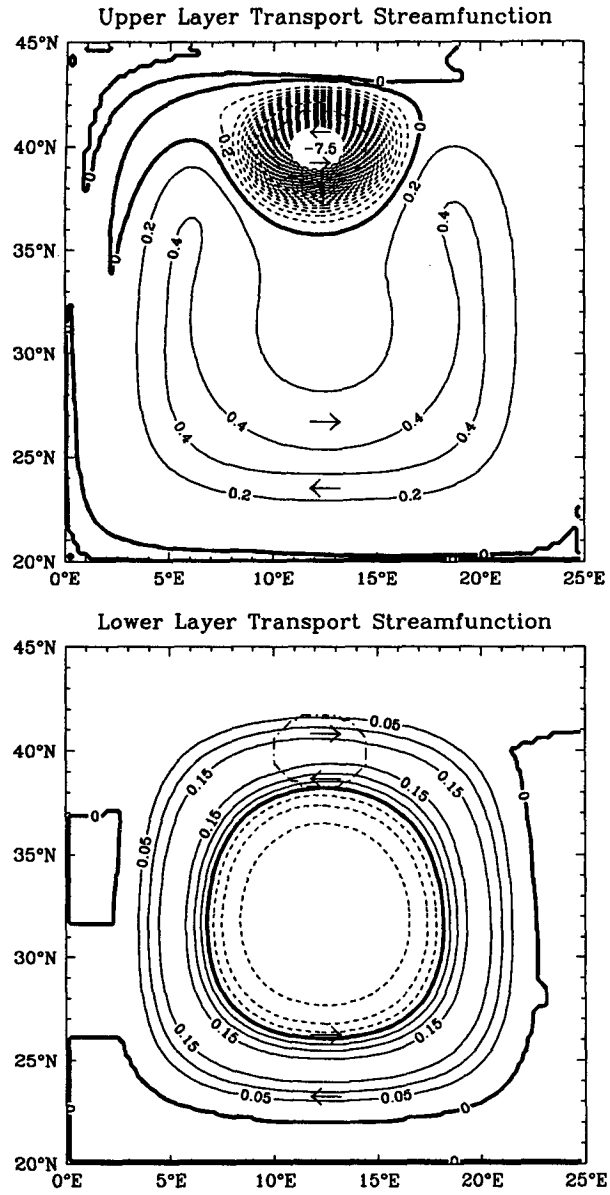

FIG. 18. Transport streamfunction of the two layers at day 1000 of FPLANE (in Sv). The dashed–dotted circles mark the forcing region.

for example, very nearly reverses the entire flow field. The present simulation is identical to EDGE except that it was forced 100 times more vigorously, giving a forcing of the magnitude of Labrador Sea Water production driving flow in the North Atlantic, and the response is no longer linear.

A rich eddy field develops in the western half of the upper layer, as seen in Fig. 19, but the lower-layer flow differs from the circulation in EDGE only in magnitude and detail, not in general form. The PV fields reveal the extent to which the eddy field modifies its environment (Fig. 20). The distortion of the upper-layer PV contours is obvious. The eddies mix PV, especially in a band near the western boundary. The explicit source of PV from the forcing creates an "island" of closed PV contours, as is familiar in studies of the PV morphology of the general circulation (e.g., Rhines 1986). The directly forced upper-layer transport streamfunction (Fig. 19) is only about 100 times as strong as in EDGE at day 100 (Fig. 8), but by day 1000 it is about 200 times as strong. The reason for the change can be found in (8). The circulation reduces the difference in PV between the two branches of the direct response, so the circulation must grow stronger to continue to have a net transport balancing the mass sink. By contrast, the lower-layer PV fields in the same figures do not vary markedly in form from their counterparts in EDGE, even though the flow is two orders of magnitude larger and the upper layer has a vigorous eddy field. This result testifies to the strong constraint put on the lower-layer flow by the large topographic PV gradients.

In the upper layer, a passive tracer is introduced in three zonal stripes. Figure 21 shows the forcing wrapping up the tracer and its advection by the paired boundary jets that reach around the basin. In the eastern part of the basin, Rossby waves gently distort the lines without disrupting them. The lines are slowly advected east to the boundary, where the tracer is eventually drawn around the basin by the eastern boundary currents. In the west the eddy field quickly obliterates the lines of tracer.

In the lower layer, there is initially no tracer, but the injected water is given a tracer concentration of 1. The lower-layer tracer (Fig. 22) initially drifts westward following the inner branch of the flow set up by the linear waves described in EDGE. Once those linear waves circumnavigate the basin, the tracer is also carried eastward from the forcing region in the outer branch of the flow, as at day 200. The two tongues pass each other, each riding along its own PV contour. The new fluid only penetrates the northwest corner of the basin after it is carried all of the way around the basin, and similarly the northeast corner of the interior is only dyed once the inner current advects fluid all of the way around the basin. Even after 1000 days, the middle of the basin does not contain any tracer. The lower-layer tracer demonstrates the stringent constraint that the strong topographic PV gradients place on exchange of fluid across isobaths in the lower layer. Also, the lower-layer tracer field clearly illustrates the difference between the (purely advective) paths taken by fluid parcels and the path along which dynamical signals propagate.

The contrast between the upper and lower layer in HIAMP demonstrates the strong constraint that the large topographic PV gradients place on eddy activity and mixing near the bottom. Once again, the deep boundary currents have paired jets. In a basin with a flat bottom the eddy activity and rate of tracer homog-

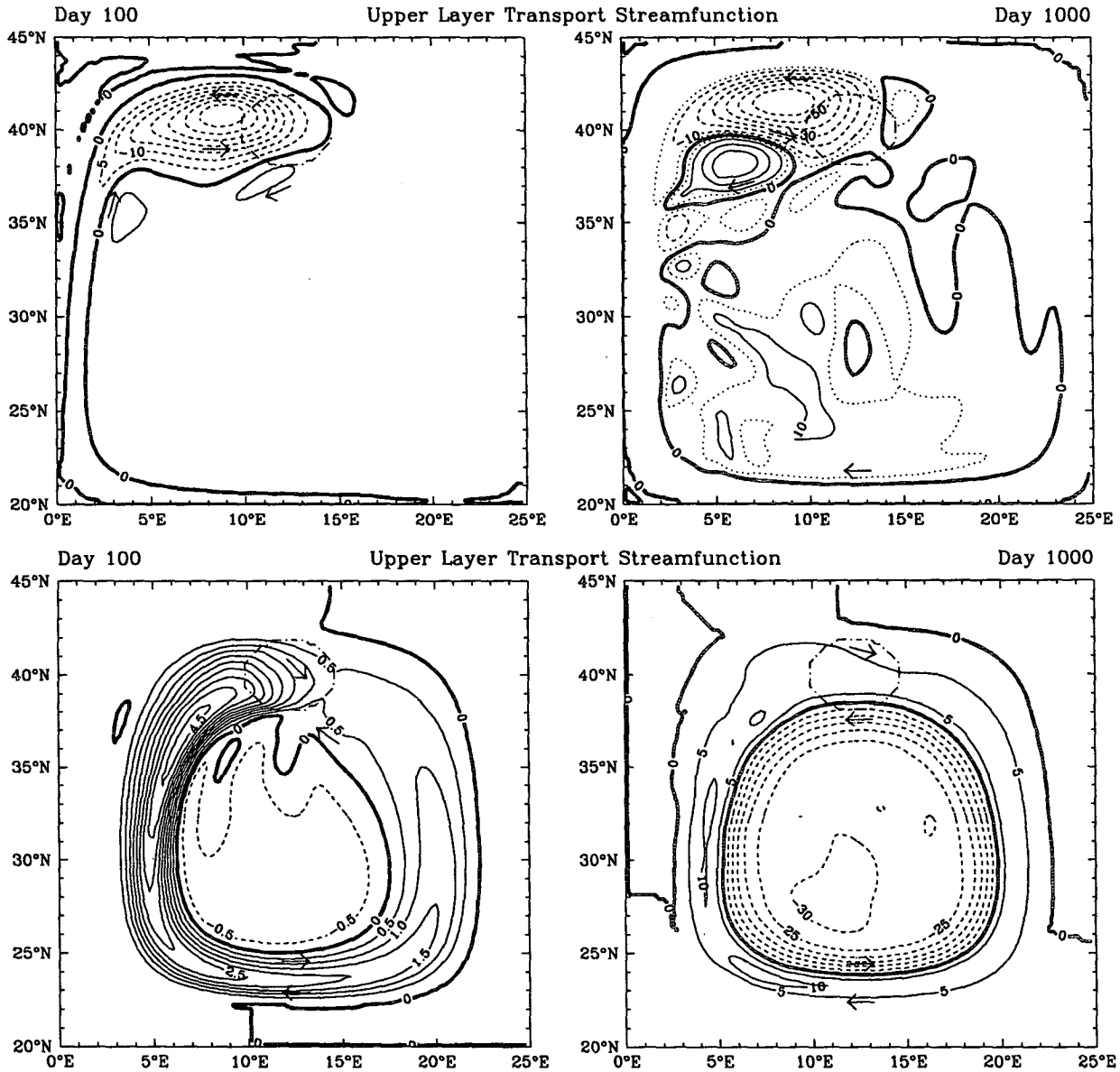

FIG. 19. Transport streamfunction (in Sv) of the two layers at days 100 and 1000 of HIAMP. Additional dotted contours have been added at −5 and 5 Sv for the upper layer at day 1000. The dashed–dotted circle marks the forcing region.

enization in the lower layer would be comparable to the upper layer, and there would only be a single deep boundary current. This simulation demonstrates that the significant impact on the flow from the sloping topography persists even for large amplitude flow.

9. Summary

A two-layer isopycnal model is used to explore the ocean's response to buoyancy forcing in a basin with sloping boundaries. Each layer develops a distinct circulation, which spins up along its PV contours. The directly forced flow in each layer is a beta plume, which is refracted to lie along PV contours. At length scales of the internal deformation radius and smaller, one layer's circulation is expressed only very weakly in the other layer. The motion is spunup by bottom-trapped topographic Rossby waves in the lower layer, planetary Rossby waves in the interior of the upper layer, and barotropic topographic Rossby waves at the edges of the upper layer.

The circulation can be decomposed locally into vertical modes, but these modes interact even in the linear limit. As a ray propagates, it encounters changing layer

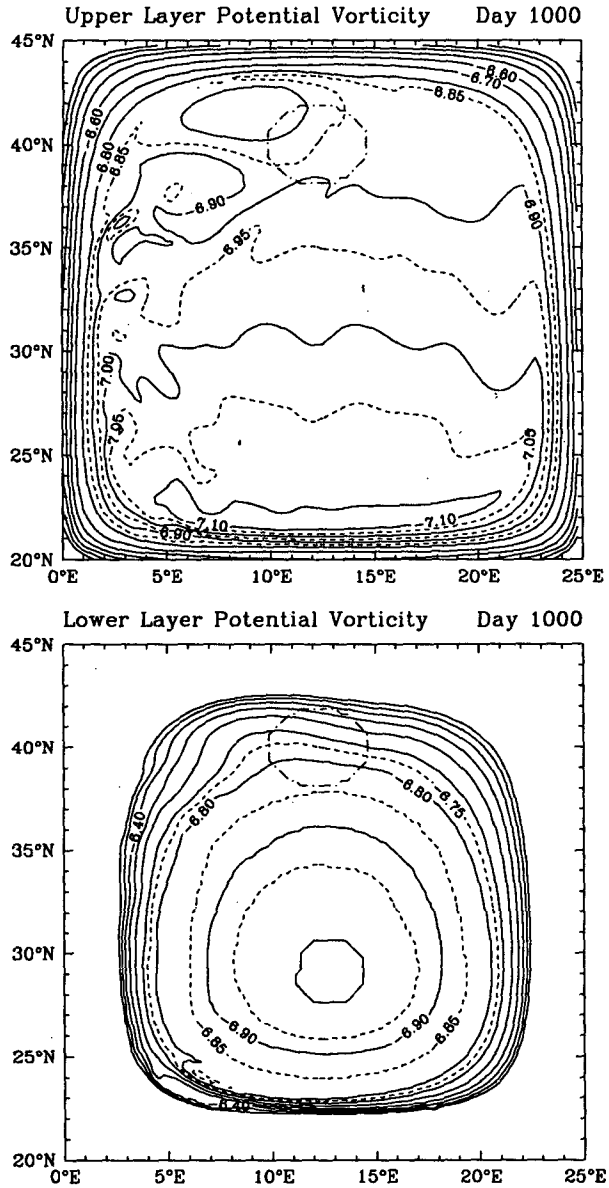

FIG. 20. Contours of $\log_{10}$PV of the two layers (in m^{-1} s^{-1}) at day 1000 of HIAMP. The dashed–dotted circles mark the forcing region.

thicknesses and bottom slopes, and its projection onto the two layers changes. Eventually the ray reaches a point in the basin where the dispersion relations of the two local modes osculate to each other. At this point the modes are coupled even for infinitesimal velocities, and energy is freely exchanged. A single ray can change from being primarily expressed in one layer and following that layer's PV contours to being primarily expressed in the other layer and following its PV contours. This change can happen quite suddenly at turning points, and provides a linear mechanism for coupling between the two layers' flows. In the absence of planetary vorticity gradients the modes remain distinct. The depth-averaged flow is only a local mode where the bottom slope is zero. A parallel result is that a baroclinic forcing can lead to a strong barotropic response for either linear or nonlinear forcing.

Numerous studies with general circulation models have shown the failure of the simple (wind driven) Sverdrup relation in regions like the subpolar gyre where buoyancy-driven flow is strong. Greatbatch et al. (1991), for example, in a diagnostic numerical model pinpoint the "JEBAR" effect as being responsible for much of the depth-integrated transport. This property, restated in the language of the present paper, is that intense buoyancy-driven flow occurs along PV contours and topography causes the paths at different depths to diverge from one another. This divergence leads to a barotropic (i.e., depth averaged) circulation even though its nature is strongly baroclinic. Much of the near-boundary flow thus involves "free jet" dynamics, with an interior responding to global requirements of mass balance.

With sloping boundaries, buoyancy forcing drives pairs of opposed boundary currents. The relative vorticity structure of these currents is characteristic of a refracted beta plume and is quite different from the structure of a Kelvin wave generated current. Likewise, the PV balance of the boundary currents as they spin up is consistent with bottom-trapped topographic Rossby waves (relative vorticity tendency and Eulerian vortex stretching combine to balance PV advection), not Kelvin waves (which would have relative vorticity tendency balancing Eulerian vortex stretching and no PV advection). The edge currents that develop in this simulation are consistent with being described as a refracted beta plume and not as a Kelvin wave induced flow. The offshore current in the lower layer is in the sense of the North Atlantic deep western boundary current and becomes more prominent than the nearshore current as the forcing is moved closer to the basin's margins. For forcing beyond the point where the second layer vanishes, the nearshore current should vanish altogether, suggesting that while the paired, opposed boundary currents might be expected for Labrador Sea Water, which is created in the interior ocean, only a single boundary current should exist in Denmark Strait overflow water.

In the simulation with a large amplitude forcing, the upper layer develops a rich eddy field and significant distortions of the PV field, as might have been expected. The lower layer, by contrast, has broad, intense flow along its PV contours, with only a weak distortion by eddies. The steady flow is persistent because of the robustness of the strong topographic PV gradients. These strong PV gradients also severely constrain mixing of fluid parcels, as demonstrated by the lower-layer tracer field. The tracer is injected with the newly formed water and is advected around the basin in two tongues that follow different PV contours. There is es-

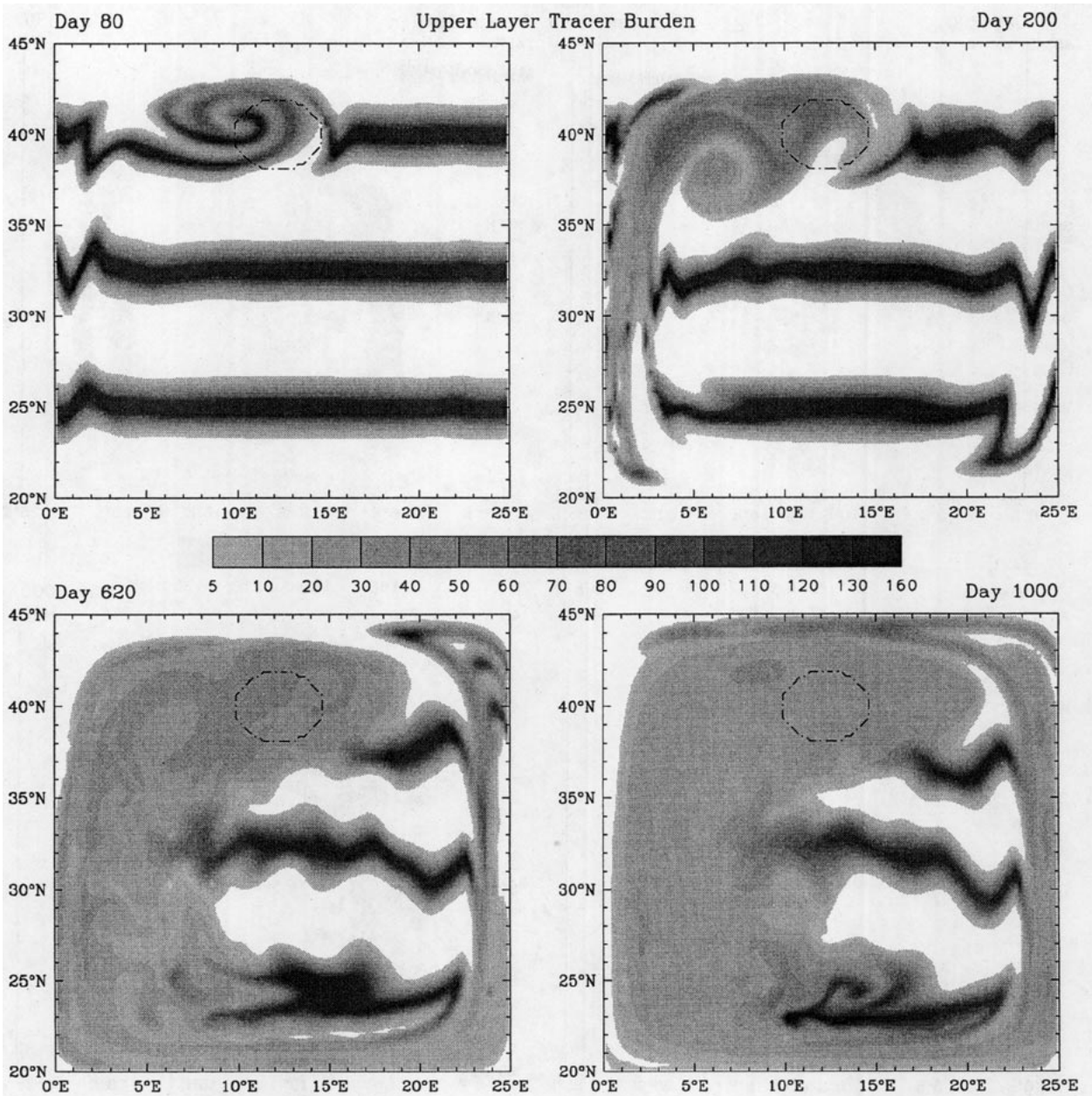

FIG. 21. Column tracer burden of the upper layer of HIAMP for days 80, 200, 620, and 1000 in arbitrary units. The dashed circles mark the forcing region.

sentially no penetration of tracer into the closed PV contours in the center of the basin. The strong topographic PV gradients in the lower layer act as a strong limit on the intensity of eddy activity in that layer and on mixing across the isopleths of PV.

All of the simulations presented here are constituted primarily of closed PV contours. In the real ocean, the slopes at the continental margins are sufficiently gentle that they do not create blocked PV contours for baroclinic flow. Most PV contours are eventually blocked by the equator. At the equator, the pairs of boundary currents feed their net mass flux into an equatorial Kelvin wave, and then is radiated into broad bottom trapped topographic Rossby waves and planetary Rossby waves at the eastern side of the basin. At the very least, these simulations should be highly pertinent to the generation of deep western boundary currents. There are even some water masses, such as Labrador Sea Water, that constitute PV minima and hence automatically have dynamically closed PV contours associated with them. It is entirely possible that some of the processes described in these simulations are pertinent to such water masses.

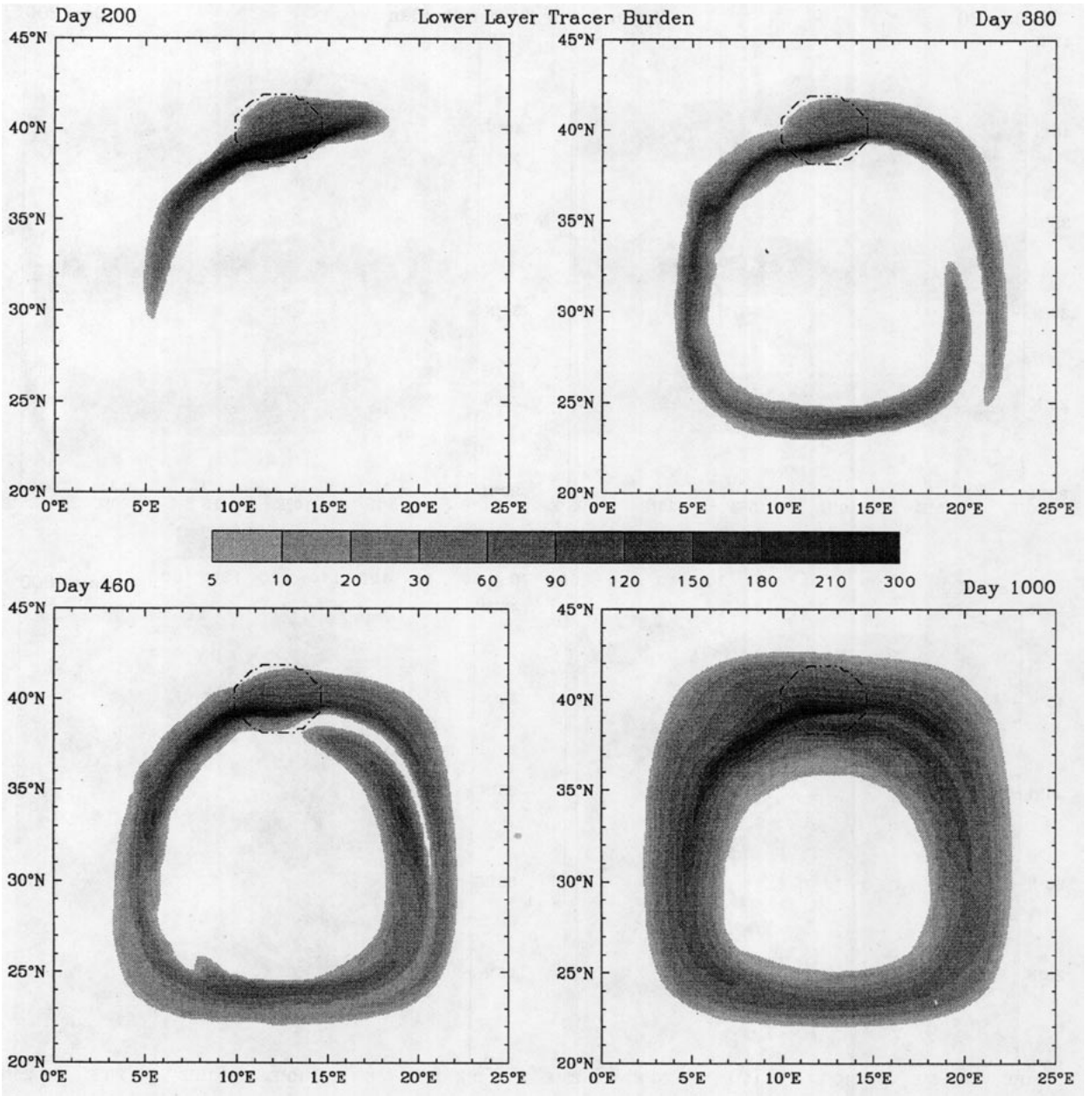

FIG. 22. Column tracer burden of the lower layer of HIAMP for days 200, 380, 460, and 1000. Upper-layer fluid is added to the lower layer with a tracer concentration of 1, so the lower-layer column tracer burden is also the thickness of upper-layer fluid in the lower layer. The dashed circles mark the forcing region.

While the present work describes only two-layer simulations, the model has been running successfully with many density layers, wind forcing, and surface outcropping of density layers. This work will be described subsequently.

Acknowledgments. The authors thank M. Kawase and L. Thompson for valuable comments which helped focus the arguments in this document. Comments from the anonymous reviewers were also helpful in clarifying certain points. This work was supported by an ONR graduate fellowship and ONR Grant N00014-92-J-1405. The figures were made with the Ferret plotting package from NOAA PMEL.

APPENDIX

The Model

All numerical simulations examined here used a two-layer shallow-water model. Each layer is of uniform

density and obeys the primitive equations for immiscible layers of incompressible Boussinesq fluid in hydrostatic balance.

For layer n with horizontal velocity $\mathbf{u}_n$ and layer thickness h_n ($n = 1$ or 2) the shallow-water momentum equation is

$$\frac{\partial \mathbf{u}_n}{\partial t} + q_n \mathbf{k} \times (h_n \mathbf{u}_n) = -\nabla B_n$$

$$- \frac{A}{h_n} \{ \nabla \cdot [h_n \nabla (\nabla^2 \mathbf{u}_n)] \} + \frac{\tau_{n-1/2} - \tau_{n+1/2}}{h_n}, \quad \text{(A1)}$$

where q_n, the layer potential vorticity, is

$$q_n = \frac{2\Omega \sin\theta + \hat{\mathbf{k}} \cdot (\nabla \times \mathbf{u}_n)}{h_n} \equiv \frac{f + \zeta_n}{h_n}. \quad \text{(A2)}$$

The Bernoulli function, B_n, is given by $B_1 = (\eta_{1/2} g'_{1/2})/\rho_0 + \frac{1}{2}\|\mathbf{u}_1\|^2$ and $B_2 = (\eta_{1/2} g'_{1/2} + \eta_{3/2} g'_{3/2})/\rho_0 + \frac{1}{2}\|\mathbf{u}_2\|^2$. Here $\eta_{n+1/2}$ is the height of the interface between layers n and $n + 1$ (the index n increases downward), and $g'_{n+1/2}$ is the reduced gravity at this interface. Momentum is diffused by a biharmonic viscosity along isopycnal layers. In spherical coordinates the biharmonic operator includes many metric terms arising from the change with latitude of the grid spacing and unit vector directions. These metric terms are smaller than the leading order terms by something proportional to the ratio of the grid spacing to the radius of the earth. Since the domain does not include the poles and the dissipation is only an arbitrary parameterization, these metric terms can be safely neglected. Apart from the diffusion parameterization, all the metric terms due to motion on a sphere are retained.

The mass conservation equation for each layer is

$$\frac{\partial h_n}{\partial t} + \nabla \cdot (h_n \mathbf{u}_n) = M_{n-1/2} - M_{n+1/2}, \quad \text{(A3)}$$

where $M_{n+1/2}$ is the externally prescribed downward diapycnal mass flux across interface $n + 1/2$.

Equations (A1)–(A3) are discretized on a staggered Arakawa C-grid, with both meridional and zonal boundaries running through the PV grid points. The momentum equations are evaluated using a vorticity advection scheme of Arakawa and Hsu (1990). This scheme conserves both total energy and potential enstrophy in the limit of nondivergent mass fluxes. While this scheme is more complicated that the vorticity advection scheme of Sadourny (1975) and does not conserve potential enstrophy and total energy in general flow, as does a scheme from Arakawa and Lamb (1981), it tolerates arbitrarily thin layers. This feature is essential for simulating either outcropping isopycnals or large amplitude topography.

The layer thickness equation is stepped using a positive definite scheme from Hsu and Arakawa (1990). This scheme is essentially the same as that of Takacs (1985) except when there is a large relative thickness difference between neighboring grid points. The Takacs scheme is second-order accurate in time and space (third-order accurate for uniform flow) and has greatly reduced phase error compared with the standard Lax–Wendroff thickness advection scheme. When there are significant thickness variations between adjacent grid points, upwind differencing advection is used, but the overall scheme retains the higher-order accuracy of the Takacs scheme. Whenever thickness falls below some prescribed thickness ϵ (here 10^{-10} m), mass is added to return the thickness to this value.

The momentum equations are time stepped using a third-order accurate scheme proposed by Matsuno (1966). Three evaluations of the time derivative are required with this scheme, but it is stable for a CFL number up to $\sqrt{3}$, which is more efficient than either a simulated backward Euler or leapfrog time stepping scheme. As an added benefit, this scheme weakly dissipates high-frequency signals. All of the high-frequency motions are relatively short gravity waves, which are not of interest. The thickness equation is stepped alternately with the integer and half-integer time step velocities in a leapfrog pattern. There is no possibility of any splitting instability, and the overall scheme is second-order accurate.

Barotropic gravity waves are resolved by this model. In these simulations the time step was extended to a reasonable value by reducing the gravity of the free surface to only 10 times the intermediate interface reduced gravity, which retards barotropic gravity wave speeds to about 12 times the baroclinic wave speeds. Tests show no significant effect of the smaller free surface reduced gravity for the simulations in the present work. In the future, there are plans to use the full barotropic gravity wave speed but to step a limited part of the barotropic equations separately with a much smaller time step than the baroclinic layer equations. This procedure is described by Bleck and Smith (1990).

In the discretized formulations for the biharmonic diffusion operator, care was taken to ensure that all layer thicknesses in the denominators also appear in the numerators in every term. This biharmonic formulation uses a flux conservative form and is formally only first-order accurate. This first-order accuracy should not be a difficulty since the value of the biharmonic diffusivity is usually decreased as the cube of the grid spacing.

In addition to the horizontal momentum diffusion within each layer, there is also a weak vertical momentum diffusion. The vertical diffusion is fully implicit, with approximately the actual molecular value of kinematic viscosity (10^{-6} m^2 s^{-1}). The purpose of this diffusion is just to control the motion of very thin layers. The momentum of layers near the bottom is completely controlled by the no-slip bottom boundary condition. At an interface the stress is given by

$$\tau_{n+1/2} = \frac{2K_\nu(\mathbf{u}_n - \mathbf{u}_{n+1})}{\min(h_{n+1}, \delta_E) + \min(h_n, \delta_E)}, \quad \text{(A4)}$$

where δ_E is a nominal Ekman layer thickness (1 m in these simulations), the idea being that viscosity-induced velocity gradients extend only a small distance into a thick homogeneous layer. At the bottom the no-slip bottom boundary condition is applied as the stress

$$\tau_{N+1/2} = \frac{2K_\nu \mathbf{u}_N}{\min(h_N, \delta_E)}. \qquad \text{(A5)}$$

With this formulation and the parameters of the simulation, a thick bottom layer has a velocity spindown time of $h_n \times 10^6$ s m^{-1}. Except where the lower layer is thin, the vertical viscosity is negligible.

In all of the simulations described here, the model is forced with an imposed cooling at the surface. This cooling is manifest as a mass flux between the two layers. The momentum of the recipient layer is diluted with the momentum of the injected fluid. All simulations here involved only two layers, but the model is able to easily incorporate an arbitrary number of isopycnal layers and forcing by a surface wind stress.

REFERENCES

Arakawa, A., and V. R. Lamb, 1981: A potential enstrophy and energy conserving scheme for the shallow water equations. *Mon. Wea. Rev.*, **109,** 18–36.

——, and Y.-J. G. Hsu, 1990: Energy conserving and potential-enstrophy dissipating schemes for the shallow water equations. *Mon. Wea. Rev.*, **118,** 1960–1969.

Bleck, R., and L. T. Smith, 1990: A wind-driven isopycnic coordinate model of the North and equatorial Atlantic Ocean; 1. Model development and supporting experiments. *J. Geophys. Res.*, **95,** 3273–3285.

Döscher, R., C. W. Böning, and P. Herrmann, 1994: Response of the circulation and heat transport in the North Atlantic to changes in thermohaline forcing in northern latitudes: A model study. *J. Phys. Oceanogr.*, **24,** 2306–2320.

Gerdes, R., and C. Köberle, 1995: On the influence of DSOW in a numerical model of the North Atlantic general circulation. *J. Phys. Oceanogr.*, **25,** 2624–2642.

Gill, A. E., and R. K. Smith, 1970: On similarity solutions of the differential equation $\psi_{zzzz} + \psi_x = 0$. *Proc. Camb. Phil. Soc.*, **67,** 163–171.

Greatbatch, R. J., A. F. Fanning, A. D. Goulding, and S. Levitus, 1991: A diagnosis of interpentadal circulation changes in the North Atlantic. *J. Geophys. Res.*, **96,** 22 009–22 023.

Hsu, Y.-J. G., and A. Arakawa, 1990: Numerical modeling of the atmosphere with an isentropic vertical coordinate. *Mon. Wea. Rev.*, **118,** 1933–1959.

Ishizaki, H., 1994: A simulation of the abyssal circulation in the North Pacific Ocean. Part I: Flow field and comparison with observations. *J. Phys. Oceanogr.*, **24,** 1921–1939.

Johnson, G. C., and J. M. Toole, 1990: Flow of deep and bottom waters in the Pacific at 10 degrees north. *Deep-Sea Res.*, **40,** 371–394.

Kawase, M., 1987: Establishment of deep ocean circulation driven by deep-water production. *J. Phys. Oceanogr.*, **17,** 2294–2317.

——, 1993: Effects of a concave bottom geometry on the upwelling-driven circulation in an abyssal ocean basin. *J. Phys. Oceanogr.*, **23,** 400–405.

——, and D. Straub, 1991: Spinup of source-driven circulation in an abyssal basin in the presence of bottom topography. *J. Phys. Oceanogr.*, **21,** 1501–1514.

Lazier, J. R. N., and D. G. Wright, 1993: Annual velocity variations in the Labrador Current. *J. Phys. Oceanogr.*, **23,** 659–678.

Matsuno, T., 1966: A finite difference scheme for time integrations of oscillatory equations with second order accuracy and sharp cut-off for high frequencies. *J. Meteor. Soc. Japan,* **44,** 85–88.

Milliff, R. F., and J. C. McWilliams, 1994: The evolution of boundary pressure in ocean basins. *J. Phys. Oceanogr.*, **24,** 1317–1338.

Oberhuber, J. M., 1993: Simulation of the Atlantic circulation with a coupled sea ice-mixed layer-isopycnal general circulation model. *J. Phys. Oceanogr.*, **23,** 808–829.

Rhines, P., 1970: Edge-, bottom-, and Rossby waves in a rotating stratified fluid. *Geophys. Fluid Dyn.*, **1,** 273–302.

——, 1977: The dynamics of unsteady currents. *The Sea.* Vol. VI, E. Goldberg, Ed., Wiley and Sons, 189–318.

——, 1983: Lectures in geophysical fluid dynamics. *Lect. Appl. Math.*, **20,** 3–58.

——, 1986: Vorticity dynamics of the oceanic general circulation. *Ann. Rev. Fluid Mech.*, **18,** 433–497.

——, 1989: Deep planetary circulation and topography: Simple models of mid-ocean flows. *J. Phys. Oceanogr.*, **19,** 1449–1470.

——, 1993: Oceanic general circulation: Wave and advection dynamics. *Modelling Oceanic Climate Interactions,* J. Willebrand and D. L. T. Anderson, Eds., Springer-Verlag, 67–149.

——, and P. MacCready, 1990: Boundary control over the large scale circulation. *Proc. Fifth 'Aha Huliko'a Hawaiian Winter Workshop on Parameterization of Small-Scale Processes,* Honolulu, HI, Hawaii Institute of Geophysics, 75–97.

Sadourny, R., 1975: The dynamics of finite-difference models of the shallow-water equations. *J. Atmos. Sci.*, **32,** 680–689.

Smith, L., 1992: Numerical simulations of stratified rotating flow over finite amplitude topography. *J. Phys. Oceanogr.*, **22,** 686–696.

Stommel, H., 1982: Is the South Pacific helium-3 plume dynamically active? *Earth Plan. Sci. Lett.*, **61,** 63–67.

——, and A. B. Arons, 1960: On the abyssal circulation of the world ocean—I. Stationary planetary flow patterns on a sphere. *Deep-Sea Res.*, **19,** 707–718.

Straub, D. N., 1990: Some effects of large scale topography in a baroclinic ocean. Ph.D. thesis, University of Washington, 164 pp.

——, and P. B. Rhines, 1989: Effects of large-scale topography on abyssal circulation. *J. Mar. Res.*, **48,** 223–253.

Takacs, L. L., 1985: A two-step scheme for the advection equation with minimized dissipation and dispersion errors. *Mon. Wea. Rev.*, **113,** 1050–1065.

Thompson, L., 1995: The effect of continental rises on the wind-driven ocean circulation. *J. Phys. Oceanogr.*, **25,** 1296–1316.

Wajsowicz, R. C., 1986: Free planetary waves in finite-difference numerical models. *J. Phys. Oceanogr.*, **16,** 773–789.

——, and A. E. Gill, 1986: Adjustment of the ocean under buoyancy forces. Part I: The role of Kelvin waves. *J. Phys. Oceanogr.*, **16,** 2097–2114.